Enhanced pedestal H-mode at low edge ion collisionality on NSTX

D. J. Battaglia (iD), W. Guttenfelder, R. E. Bell (iD), A. Diallo, N. Ferraro (iD), E. Fredrickson, S. P. Gerhardt, S. M. Kaye, R. Maingi, and D. R. Smith

View Online   Export Citation   CrossMark

ARTICLES YOU MAY BE INTERESTED IN

A new explanation of the sawtooth phenomena in tokamaks
Physics of Plasmas **27**, 032509 (2020); https://doi.org/10.1063/1.5140968

When does turbulence spreading matter?
Physics of Plasmas **27**, 042308 (2020); https://doi.org/10.1063/1.5117835

Design study of a combined interferometer and polarimeter for a high-field, compact tokamak
Physics of Plasmas **27**, 042516 (2020); https://doi.org/10.1063/1.5142638

Enhanced pedestal H-mode at low edge ion collisionality on NSTX

View Online   Export Citation   CrossMark

D. J. Battaglia,[1,a),b)] (iD) W. Guttenfelder,[1] R. E. Bell,[1] (iD) A. Diallo,[1] N. Ferraro,[1] (iD) E. Fredrickson,[1] S. P. Gerhardt,[1]
S. M. Kaye,[1] R. Maingi,[1] and D. R. Smith[2]

AFFILIATIONS

[1]Princeton Plasma Physics Laboratory, Princeton, New Jersey 08543, USA
[2]Department of Engineering Physics, University of Wisconsin – Madison, Madison, Wisconsin 53706, USA

Note: This paper is part of the Special Collection: Papers from the 61st Annual Meeting of the APS Division of Plasma Physics.
Note: Paper JI2.3.
[a)]Invited speaker.
[b)]Author to whom correspondence should be addressed: dbattagl@pppl.gov

ABSTRACT

The Enhanced Pedestal (EP) H-mode regime is an attractive wide-pedestal high-β_P scenario for the National Spherical Torus Experiment Upgrade (NSTX-U) and next-step devices as it achieves enhanced energy confinement ($H_{98y,2} > 1.5$), large normalized pressure ($\beta_N > 5$), and significant bootstrap fraction ($f_{BS} > 0.6$) at $I_P/B_T = 2$ MA/T. This regime is realized when the edge ion collisionality becomes sufficiently small that a positive feedback interaction occurs between a reduction in the ion neoclassical energy transport and an increase in the particle transport from pressure-driven edge instabilities. The EP H-mode was most often observed as a transition following a large edge-localized mode in conditions with low edge neutral recycling. It is hypothesized that the onset of pressure-driven instabilities prior to the full recovery of the neutral density leads to a temporary period with an elevated ion temperature gradient that triggers the transition to EP H-mode. Linear CGYRO and M3D-C1 calculations are compared to beam emission spectroscopy and magnetic spectroscopy in order to describe the evolution of the edge particle transport mechanisms during the ELM recovery and the saturated EP H-mode state. The observations are consistent with the hypothesis that the onset of pressure-driven edge instabilities, such as the kinetic ballooning mode and kink-peeling mode, can be responsible for the increased particle transport in EP H-mode.

I. INTRODUCTION

The size and capital cost of a tokamak fusion reactor are projected to be reduced by realizing compact plasma confinement devices that operate with a large fusion power density and low recirculating power.[1,2] The fusion power density is the ratio of the fusion power (P_{fus}) over the plasma volume (V_P), and it scales strongly with the toroidal magnetic field strength (B_T) and the plasma toroidal β_T ($\beta_T = 2\mu_0\langle p\rangle/B_T^2$): $P_{fus}/V_P \propto B_T^4\beta_T^2 \propto \langle p\rangle^2$, where $\langle p\rangle$ is the average plasma pressure. The desire to maximize $\langle p\rangle$ in compact reactors favors operating at a significant fraction of the Greenwald density limit ($f_{GW} = n_e/n_{GW} = \pi a^2 n_e/I_p$). Achieving the necessary reduction in the recirculating power requires plasma confinement regimes with energy confinement that significantly exceeds standard H-mode confinement ($H > 1.5$), suitable particle transport to remove plasma impurities, and a large fraction of self-driven toroidal current (i.e., bootstrap current fraction or f_{BS}). Furthermore, the target regimes must not have large

edge-localized mode (ELM) instabilities (i.e., ELM-free) in order to avoid damage to the plasma facing components (PFCs) from large, transient heat fluxes.

The spherical tokamak (ST) reduces the aspect ratio of the magnetic geometry ($A = R/a < 2$) in order to increase stability at larger β_T at the expense of the achievable B_T for a fixed plasma volume compared to conventional-A tokamaks ($A \sim 3$). A key mission of the National Spherical Torus Experiment (NSTX) and the follow-on device under construction (NSTX-U)[3] is to contribute critical data required to optimize the aspect ratio of future tokamak reactors. A unique characteristic of the ST geometry is the realization of regimes that simultaneously achieve high β_T and high β_P ($\beta_P = \beta_T B_T^2/B_P^2$) with a low central safety factor (q_0). These regimes provide a promising route for realizing a compact tokamak fusion reactor with a large fusion power density, enhanced energy confinement, and large f_{BS} ($f_{BS} \sim \beta_P/A^{1/2}$).

High β_p regimes on conventional-A tokamaks realize enhanced energy confinement via the stabilization of ion-temperature-gradient (ITG) driven transport by the large edge magnetic shear with increased flux compression at the outboard midplane due to a large Shafranov shift ($\Delta/r \propto \beta_p/A$).[4,5] Substantial experimental and theoretical work has demonstrated that the suppression of ITG instabilities in tokamaks leads to ion energy transport that approaches the theoretical minimum established by neoclassical transport.[6] High β_p regimes on conventional-A devices have demonstrated enhanced energy confinement ($H_{98y,2} > 1.5$) at large f_{GW} and f_{BS}, with β_T on the order of 2%.[7,8] Reducing the aspect ratio of the magnetic geometry accesses the attractive high β_p regime with β_T on the order of 20% in STs. Operating at larger β_T has the potential to reduce the size of a fusion reactor based on the high β_p regime.

Experimental and theoretical work for STs has shown that ion thermal transport is often consistent with neoclassical theory in the region of large magnetic shear in H-mode.[9–11] The agreement with neoclassical theory is attributed both to the suppression of ITG instabilities and the enhancement of neoclassical transport due to wide trapped particle orbits. Conversely, electron energy transport is dictated by either electrostatic or electromagnetic drift-wave, energetic particle and magneto-hydrodynamic (MHD) instabilities.

The Enhanced Pedestal (EP) H-mode regime[12] on NSTX is an attractive regime for compact, steady-state, tokamak reactor concepts since it achieves enhanced confinement ($H_{98y,2}$ as large as 1.8[13]) in an ELM-free regime at large volume-averaged values for β_T ($\beta_T \sim 20\%$), Greenwald density fraction ($f_{GW} > 70\%$), and β_p ($\beta_p \sim 1.6\%$). The defining feature of EP H-mode is a dramatic increase in the magnitude of the ion temperature gradient (∇T_i) near the plasma edge that leads to larger core plasma temperatures. At the same time, the particle confinement is degraded such that the secular rise in the plasma density typical of ELM-free operation is reduced or completely arrested. This paper presents evidence that the improved energy confinement observed in EP H-mode is due to a reduction in the neoclassical ion diffusivity ($\chi_{i,neo}$) with smaller ion collisionality (ν_i^*), while the degraded particle confinement is attributed to pressure-driven MHD instabilities that act to maintain a constant edge pressure profile as $|\nabla T_i|$ increases.

The largest lever for reducing the edge ν_i^* on NSTX is the mitigation of wall recycling. Maingi *et al.* first described an EP H-mode discharge (117820) produced on NSTX in 2005[12] that occurred early in an experiment with deuterium plasmas that followed extended operations with helium plasmas. The helium plasma operation reduced the inventory of deuterium gas within the carbon plasma facing components (PFCs) resulting in low deuterium wall recycling conditions for the first few deuterium plasma discharges of the experiment. This permitted access to EP H-mode without the use of lithium wall coatings.

The first use of inter-shot solid lithium coatings on the carbon PFCs in 2008 increased the occurrence of EP H-mode in NSTX operations. A paper by Maingi *et al.* compares the first highly shaped discharges with lithium wall coatings,[14] and the dataset includes an EP H-mode discharge (132588) that was described in detail in a subsequent paper.[15] The connection between EP H-mode and low wall recycling conditions was reinforced in a publication by Maingi *et al.*[13] describing an EP H-mode discharge (134991) with large normalized energy confinement ($H_{98y,2} = 1.8$) that occurred during operations with routine lithium wall coatings in 2009. One unique feature of this discharge is that most of the active neutral fueling is provided by the supersonic gas injector,[16] which improves the fueling efficiency and significantly reduces the neutral pressure in the vacuum region compared to the standard fueling valves on NSTX. Access to low edge ν_i^* also benefits from a reduction of the edge Z_{eff}; consequently, EP H-mode was more likely to occur in conditions that reduced the impurity content in the edge region.

A number of observations concerning EP H-mode were described by Gerhardt *et al.*[17] by examining about 50 different discharges with H-mode and EP H-mode phases. The analysis demonstrated that EP H-mode could occur over a broad range of magnetic geometries (plasma boundary shape, I_p, B_T, and q_{95}), with and without the application of non-axisymmetric non-resonant magnetic fields, and with different PFC conditioning (boron and lithium surface coatings on carbon PFCs). Furthermore, it was shown that EP H-mode could occur at different times within the discharge evolution and was most often observed experimentally following a large ELM. The EP H-mode phase persisted after the ELM recovery provided the discharge remained within stability limits as the stored energy increased. It was also found that in EP H-mode the core T_i/T_e ratio typically increases compared to standard H-mode regimes, the location of steepest $|\nabla T_i|$ could occur at different positions within the pedestal, the magnitude of the carbon rotation gradient ($|\nabla v_C|$) increased concurrently with the increase in $|\nabla T_i|$, and that the location of the maximum $|\nabla v_C|$ and radial electric field gradient ($|\nabla E_r|$) occurred more inboard of the steepest $|\nabla T_i|$.

The work presented in this paper builds on the previous observations and analysis by presenting a more detailed description of the transport processes responsible for the enhanced confinement in EP H-mode. Section II presents a detailed comparison between H-mode and EP H-mode on NSTX in order to review the defining features of EP H-mode. Section III demonstrates that the improved thermal confinement in EP H-mode is due to the reduction of neoclassical ion thermal transport as the edge ν_i^* is reduced. Specifically, at low deuterium collisionality ($\nu_i^* < 0.3$), the banana-regime neoclassical thermal transport decreases rapidly with lower collisionality. This is demonstrated using a database of H-mode discharges on NSTX and a simple 1D transport model assuming purely ion neoclassical thermal transport. Section IV characterizes the role of an ELM in initiating a bifurcation where the edge density decreases to maintain a nearly constant pressure profile as $|\nabla T_i|$ increases with smaller ν_i^*. A key feature of the bifurcation is the presumed existence of a pressure-driven MHD-like instability that has a larger fractional impact on the total particle transport compared to the total energy transport within the pedestal. Section V uses pedestal measurements compared to linear gyrokinetic and resistive fluid MHD calculations to gain insight into the pedestal transport mechanisms in the wide-pedestal and EP H-mode regimes. The data and analysis support the proposed bifurcation mechanism where the particle transport increases as the nature of the ion-scale instabilities becomes more MHD-like in EP H-mode. Section VI briefly describes the global stability properties of EP H-mode and discusses the opportunity for accessing and optimizing EP H-mode on NSTX-U and higher-field devices. The final section, Sec. VII, presents a brief summary and proposes activities required for confident extrapolation of EP H-mode to long-pulse, enhanced-confinement scenarios in high-β_p regimes.

II. COMPARISON OF WIDE PEDESTAL H-MODE AND EP H-MODE ON NSTX

A wide-pedestal H-mode regime was routinely achieved on NSTX by reducing the deuterium wall recycling of the carbon PFCs using inter-shot helium glow discharge cleaning followed by evaporative lithium coatings.[14,18–20] Interpretive analysis of discharges with and without lithium conditioning on NSTX established that the recycling rate decreased from about 0.98 with boron wall coatings to about 0.9 with solid lithium wall coatings.[21] The reduction in the edge neutral density leads to a wider density gradient region with a smaller plasma density gradient, altering the nature of the dominant anomalous thermal and particle transport mechanisms in the pedestal. Most notably, the electron temperature (T_e) pedestal width expands as micro-tearing (MT) instabilities are suppressed in the regions with appreciable density gradients, and $|\nabla T_e|$ increases to a level set by the onset of hybrid trapped electron mode (TEM) and kinetic ballooning mode (KBM) instabilities.[15,20] The TEM-KBM hybrid instabilities share some defining features with the theoretical descriptions of each instability that may indicate that there is a competition between different branches of modes.[15] Electron temperature gradient (ETG) instabilities also contribute to the electron energy transport at the bottom of the pedestal and are most likely responsible for maintaining a nearly stiff $|\nabla T_e|$ near the plasma boundary. The reduction in the particle source and the changes to the anomalous transport characteristics in the wide-pedestal regime leads to an inward shift of the pressure gradient facilitating ELM-free operation. The reduction of neutral fueling resulting in an inward shift of the pressure pedestal and improved ELM stability is consistent with conventional-A devices in regimes where the electron density pedestal location is in inside the temperature pedestal location.[22] While the wide pedestal H-mode regime demonstrated improved global energy confinement ($H_{98y,2} > 1$), a significant drawback was the secular rise in the impurity density and radiated power if the regime was sustained without ELMs.[23,24]

EP H-mode was observed when the edge density was reduced even further resulting in enhanced energy and momentum confinement compared to the wide-pedestal H-mode regime. The red trace in Fig. 1 shows an example of discharge with a 300 ms EP H-mode phase (gray shading) compared to a nearly matched ELM-free wide-pedestal H-mode discharge (blue). These discharges have a similar near-double-null shape, $I_p = 0.9$ MA, $B_T = 0.45$ T, $P_{NBI} = 3$ MW, and q_{95} ~ 9 (see Figs. 4 and 7 in Ref. 17) and inter-shot lithium wall conditioning. The most significant operational difference between the two discharges is that the amplitude of an applied non-resonant 3D magnetic field is 25% larger in 141133 (red) compared to 141125 (blue). Previous analysis of EP H-mode focused on comparing pre- and post-ELM time periods in order to compare H-mode and EP H-mode states. The analysis throughout this paper uses the matched discharges shown in Fig. 1 in order to facilitate comparisons at matched line-averaged density over longer time-averaging windows.

EP H-mode phases were usually observed following the recovery from a large ELM, as demonstrated in Fig. 1. In 141133 (red traces), two large ELM events deliver heat pulses to the PFCs and liberate bursts of neutral gas from the material surfaces as inferred from the D_α emission from the divertor [Fig. 1(b)]. Following the second ELM (0.65 s), the confinement time increases [Fig. 1(a)] to a larger level compared to the H-mode discharge (blue) during similar ELM-free and MHD quiescent [Fig. 1(c)] periods. The EP H-mode phase ends
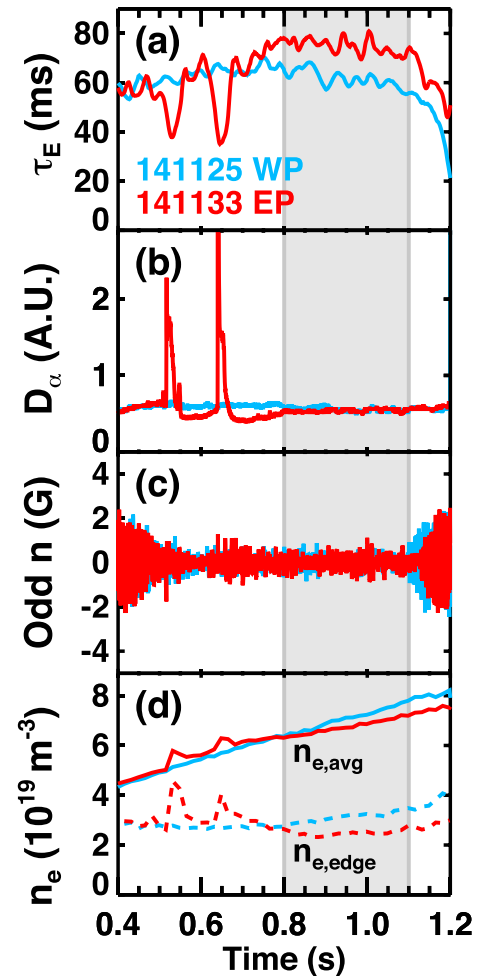

FIG. 1. Shaded region compares an EP H-mode phase (red) to a matched wide pedestal (WP) H-mode (blue) where the (a) global energy confinement is elevated. The comparison is made in a phase without (b) ELMs and (c) large-scale MHD. (d) The line-averaged density (solid) increases at a slower rate in the EP H-mode phase due to a reduction in the edge density (dashed).

with the appearance of core MHD typically associated with the onset of a 2/1 mode coupled with a 1/1 kink as the central q decreases toward unity.[25] Figure 1(d) illustrates that the enhanced thermal confinement occurs concurrently with a beneficial reduction in the rate of density accumulation during the ELM-free phase, particularly in the edge of the plasma where the solid line shows the line-averaged midplane electron density (n_e) while the dashed line shows the n_e near the edge ($\psi_N = 0.9$) at the outboard midplane. The improvement in energy confinement time and the normalized energy confinement between the wide pedestal H-mode ($H_{98y,2} \sim 1.2$) and EP H-mode ($H_{98y,2} \sim 1.35$) is not as dramatic as other examples of EP H-mode;[13] however, the modest increase in the core pressure is conducive to maintaining a long EP H-mode period that remains below MHD stability limits with $\beta_N \sim 5$ and $\beta_N/l_i \sim 10$ using a fixed P_{NBI} and no active β_N or resistive wall mode (RWM) control.

The two discharges shown in Fig. 1 have a constant non-resonant $n = 3$ field in addition to the odd-n error field correction (EFC) field[26] applied using six ex-vessel window-frame coils at the outboard midplane after 0.4 s. The blue and red traces have a non-resonant $n = 3$ field applied using a maximum amplitude of 400 A and 500 A on the window-frame coils, respectively. Increasing the $n = 3$ current amplitude in the window-frame coils to 600 A resulted in a discharge with regularly spaced ELMs. Thus, the 500 A case (red) is close to the threshold for consistently inducing ELMs that would otherwise prevent the evolution of the pedestal to the EP H-mode state. Previous work has found that the ELM onset on NSTX is attributed to edge-current-driven low-n kink-peeling modes.[19,27] The close proximity of the 3D field strength to the level needed to induce regular ELMs suggests that the two example discharges in Fig. 1 operate near a kink-peeling stability boundary.

Non-resonant $n = 3$ fields alter the edge transport and provide a useful actuator for altering the properties of the pedestal on NSTX.[24] Figure 2 presents midplane profiles for the two discharges in Fig. 1 (red and blue) in addition to a third matched discharge that only

applies 3D fields for EFC (black). The three matched discharges are from the same experiment, and the 70 ms time-ranges used for the profile comparisons are chosen to match the line-averaged density (within 3%) during ELM-free and MHD-quiescent phases. All of the profiles are plotted versus the normalized poloidal flux derived from kinetic equilibrium fits with a constraint on the separatrix T_e.

The left column of Fig. 2 presents experimental measurements made using the Multi-Point Thomson Scattering (MPTS) diagnostic[28] [Figs. 2(a) and 2(b)] and the Charge-Exchange Spectroscopy system (CHERS) diagnostic measuring fully stripped carbon[29] [Figs. 2(c)–2(e)]. Both diagnostics image the plasma at the device midplane. The analysis in this paper assumes that the ion temperature (T_i) is equivalent to the measured carbon temperature [Fig. 2(c)]. The carbon poloidal flow[29] (not shown) is measured to be small (within ± 1 km/s) across the pedestal profile. The shaded region indicates the pedestal region as determined from the electron temperature profile.

The right column of Fig. 2 shows profiles derived from the fits to the measurements within the shaded range in the left column. The radial electric field [Fig. 2(f)] is derived from force-balance using the CHERS measurements. The deuterium density (n_D) [Fig. 2(g)] and effective ion charge, Z_{eff} [Fig. 2(h)], are derived assuming that the only impurity ion is fully stripped carbon since the lithium content of plasmas on NSTX is found to be much smaller than the carbon content in the wide-pedestal regime.[30,31] Figure 2(i) shows the electron pressure, P_e (dashed), and the sum of P_e plus the ion pressure (solid). The final panel, Fig. 2(j), shows the difference between the ion and electron temperature.

The impact of non-resonant fields below the ELM triggering threshold on the pedestal structure in wide-pedestal H-modes on NSTX is highlighted by comparing the blue and black traces. The imposed fields have the largest impact around $\psi_N = 0.9$ with a reduction of the carbon toroidal rotation ($v_{C,tor}$) [Fig. 2(e)] and E_r due to neoclassical toroidal viscosity. Another significant impact is the inward shift of the carbon density pedestal (n_C) [Fig. 2(d)] and a broadening of the inferred n_D that reduces the edge Z_{eff} for $\psi_N > 0.7$. The T_e profiles [Fig. 2(a)] in the blue and black discharges are very similar, and the T_i profile exhibits lower separatrix temperatures with the applied field, but matched core T_i [Fig. 2(c)].

The red traces demonstrate the defining characteristics of EP H-mode, particularly compared to the blue traces where both discharges have finite non-axisymmetric field offset from the level needed for EFC. At the bottom of the pedestal ($\psi_N > 0.8$), the T_e profile is relatively stiff, and the average ion temperature gradient is larger, while, at the top of the pedestal ($0.6 < \psi_N < 0.8$), the average T_e gradient is larger. The increase in the edge T_e and T_i temperature gradients in the EP H-mode discharge results in larger core temperatures and a larger difference in the core T_i and T_e as shown in Fig. 2(j). The electron [Fig. 2(b)], carbon [Fig. 2(d)], and deuterium [Fig. 2(g)] densities are reduced in the edge region, implying a more peaked density profile with a larger density in the core since the line-averaged density is matched for all three discharges. The lower edge density and larger temperatures result in a similar pressure profile for $\psi_N > 0.7$ [solid lines in Fig. 2(i)]. The minimum in the E_r shifts inward, increasing the E_r gradient near $\psi_N = 0.85$, consistent with previous comparisons of H-mode and EP H-mode discharges.[12,13,17]

Figure 3 further summarizes the properties of the EP H-mode discharge (red) compared to the wide pedestal H-mode (blue and

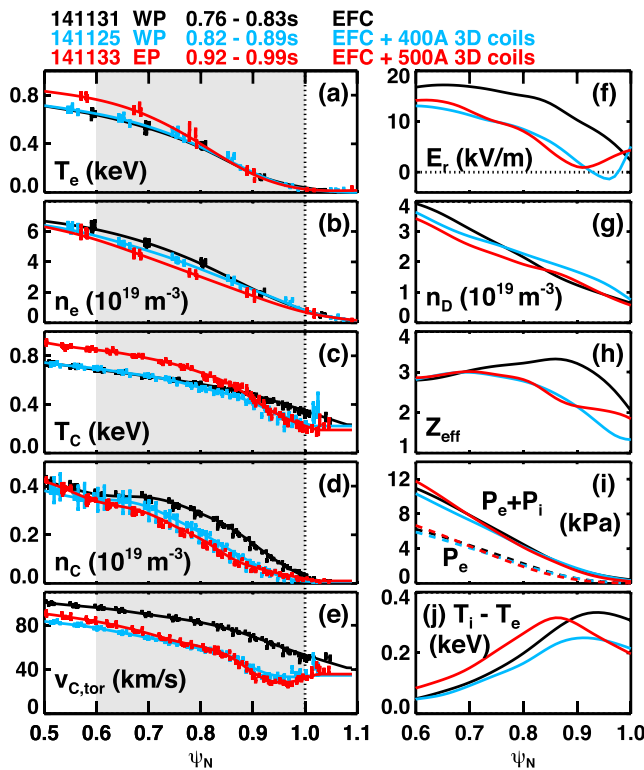| 141131 | WP | 0.76 - 0.83s | EFC |
| 141125 | WP | 0.82 - 0.89s | EFC + 400A 3D coils |
| 141133 | EP | 0.92 - 0.99s | EFC + 500A 3D coils |

FIG. 2. Comparison of midplane profiles for an EP H-mode phase (red) with non-resonant $n = 3$ fields to wide-pedestal H-mode discharges with (blue) and without (black) non-resonant $n = 3$ fields. Plots in the left column include diagnostic measurements with error bars (points) and a fit (solid lines): (a) electron temperature, (b) electron density, (c) carbon temperature, (d) carbon density, and (e) carbon toroidal rotation. Plots in the right column are derived from the measurement fits within the gray region: (f) radial electric field, (g) inferred deuterium density, (h) Z_{eff}, (i) electron pressure (dashed) and sum of ion and electron pressure (solid), and (j) difference in ion and electron temperature.

black) using the same discharges as Fig. 2. The electron density profile is more peaked in the EP H-mode discharge due to a reduction in $-\nabla n_e$ near the separatrix and an increase near the top of the pedestal [Fig. 3(a)]. The EP H-mode phase achieves metrics beyond what is typical for H-mode operations on NSTX: the maximum $-\nabla T_i$ is greater than 0.1 keV/cm [Fig. 3(b)], and the ion collisionality [Fig. 3(c)] in the pedestal is below 0.3. The lower collisionality near $\psi_N = 0.9$ is driven by the lower density, while farther inside the collisionality is lower due to the larger T_i at the top of the pedestal. Figure 3(d) shows the absolute value of ∇E_r to illustrate that the peak in $-\nabla T_i$ occurs in a region of small $|\nabla E_r|$ as noted in previous publications.[17] This observation reinforces that the differences in ∇T_i are not driven by a local change to the $E \times B$ shear. However, as will be shown in later sections, the increase in $|\nabla E_r|$ for $0.7 < \psi_N < 0.8$ may contribute to the larger $-\nabla n_e$ at the top of the pedestal that contributes to a more peaked density profile. The final panel, Fig. 3(e), shows that the reconstruction of the q-profile that is constrained by the MSE diagnostic[32] is similar for the three discharges highlighting that the
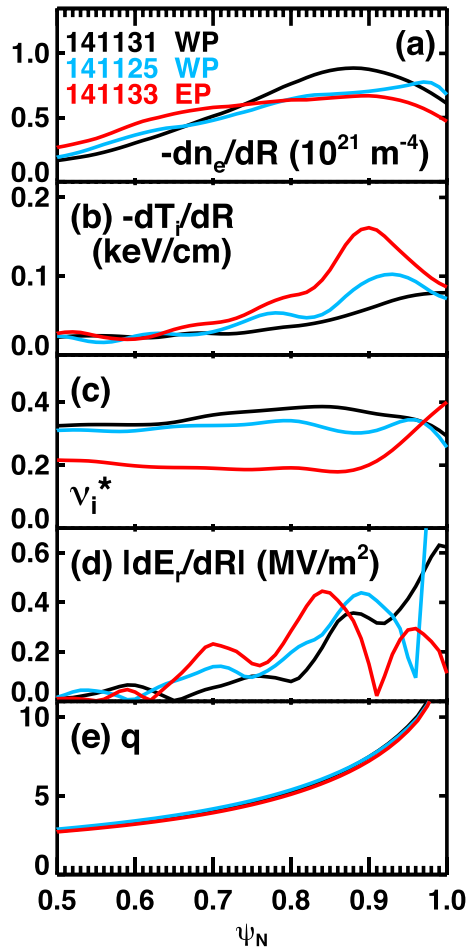

FIG. 3. (a) Electron density gradient, (b) ion temperature gradient, (c) deuterium collisionality, (d) the magnitude of the radial electric field gradient, and (e) the q-profiles for the same discharges as Fig. 2.

changes in the transport are not attributed to changes in the magnetic shear.

The motivation for the analysis described in this paper is to better understand the changes in the edge transport that give rise to the larger edge temperature gradients and improved thermal confinement with the concurrent decrease in the particle confinement in 141133 (red) compared to 141125 (blue). The next section will demonstrate that the improved energy confinement is due to a marked reduction in the ion neoclassical diffusivity due to a reduction in the edge ion collisionality.

III. NEOCLASSICAL ION THERMAL TRANSPORT AT LOW EDGE ION COLLISIONALITY

The increase in the ion temperature gradient in the plasma edge with lower collisionality is consistent with banana-regime neoclassical transport being the dominant energy transport mechanism for the deuterium ions in the pedestal region. Previous analysis has demonstrated that the large edge ion temperature gradients measured in EP H-mode exceed the maximum gradients predicted using analytical neoclassical theory and the experimentally inferred ion heat flux.[17] The over-prediction of the neoclassical heat flux compared to the experimentally inferred heat flux provides further confidence that anomalous ion thermal transport is significantly less than the neoclassical ion thermal transport in the range of collisionality considered.

Demonstration of quantitative agreement between the measured and predicted ion neoclassical heat flux is an on-going activity where the primary focus is to examine the sensitivity of the assumptions used in calculations. For example, the impact of multi-species, non-local, and non-Maxwellian effects on the neoclassical predictions is under consideration. Also, effort is directed at understanding the impact of assumptions typically made to infer the experimental heat flux. For example, recent measurements of the deuterium temperature (T_D) at DIII-D have demonstrated that $T_e < T_D < T_C$ in the H-mode pedestal leading to larger inferred ion energy flux (due to smaller i-e collisional energy transfer) compared to calculations that assume $T_D = T_C$.[33] The focus of this section is to demonstrate that the increased magnitude of ∇T_i at low ion collisionality (ν_i^*) in the EP H-mode pedestal is consistent with the predicted *scaling* of neoclassical theory where $\chi_{i,neo} \propto \nu_i^*$. Thus, the transition to the EP H-mode can be independent of the details of the anomalous ion energy transport.

Analytical neoclassical theory predicts the leading order term of the ion thermal diffusivity for a single ion species in the banana regime is

$$\chi_{i,neo} \propto \frac{\varepsilon^{-\frac{3}{2}} q^2 \rho_i^2}{\tau_i},\qquad(1)$$

where ε is the inverse aspect ratio, q is the local safety factor, ρ_i is the ion Larmor radius, and τ_i is the ion-ion collision time. Assuming different Maxwellian ion species with disparate Z and M, $\chi_{i,neo}$ scales as[34]

$$\chi_{i,neo} \propto \frac{q^2}{\varepsilon^{3/2}}\left(\frac{n_i Z_i^2}{M_i^{1/2}} + \sqrt{2}\sum_Z \frac{n_Z Z_Z^2}{M_Z^{1/2}}\right)\frac{M_i}{B^2}\frac{\ln\Lambda_i}{T_i^{1/2}},\qquad(2)$$

where subscript i describes a single ion species and subscript Z describes all of the other ion species. In Eq. (2), B is the ensemble-averaged magnetic field and $ln\Lambda_i$ is the Coulomb logarithm.

The total ion neoclassical heat flux from all ion species is

$$q_{i,neo} = -\sum_i n_i \chi_{i,neo} \frac{dT_i}{dR}. \qquad (3)$$

Substituting Eq. (2) into Eq. (3) and assuming that T_i and ∇T_i are the same for all ion species, deuterium and fully ionized carbon are the primary ion species and enforcing $Z_{eff} < 3$, it is found numerically that

$$q_{i,neo} = -\nabla T_i \sum_i n_i \chi_{i,neo} \propto -\frac{dT_i}{dR} \frac{q^2}{B^2 \varepsilon^{3/2}} \frac{Z_{eff} n_e^2}{T_i^{1/2}}. \qquad (4)$$

With a fixed plasma shape, Eq. (4) approximately scales as

$$q_{i,neo} \propto -\nabla T_i \frac{Z_{eff} n_e^2}{I_p^2 T_i^{1/2}} \propto -\nabla T_i \frac{Z_{eff}}{T_i^{1/2}} \left(\frac{n_e}{n_{GW}}\right)^2, \qquad (5)$$

where n_{GW} is the Greenwald density limit. Equation (5) demonstrates that for a fixed plasma geometry and neoclassical ion heat flux ($q_{i,neo}$), $-\nabla T_i$ increases with I_p and with smaller n_e or a more pure plasma ($Z_{eff} \rightarrow 1$).

Figure 4(a) plots the terms on the right-hand side of Eq. (4) for the three discharges shown in Figs. 2 and 3. The profiles are similar for $\psi_N > 0.85$ indicating that the differences in the edge ion temperature gradients [Fig. 3(b)] are consistent with the neoclassical scaling with the edge $Z_{eff} n_e^2 T_i^{-1/2}$ [Fig. 4(b)]. In other words, the increased $-\nabla T_i$ in the EP H-mode phase (red) near $\psi_N = 0.9$ is consistent with the
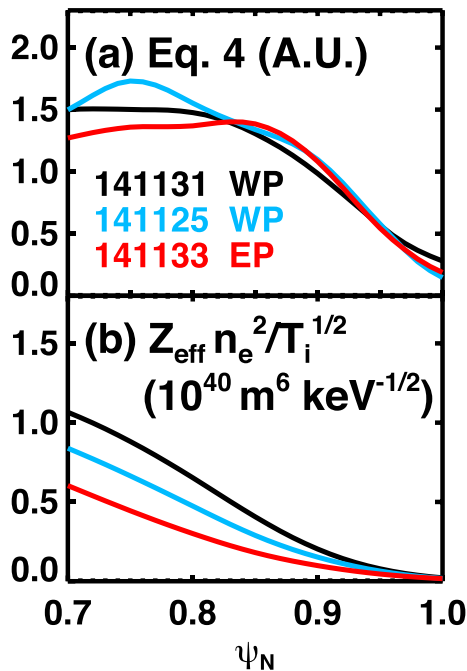
expected scaling of banana-regime neoclassical transport with reduced edge n_e.

Further evidence for the agreement of the scaling of ∇T_i with the leading-order neoclassical scaling is demonstrated using a large database from NSTX. The database is formed by identifying the location of the maximum edge $-\nabla T_i$ in every CHERS profile measured when the neutral beam injection power is at least 2 MW during the operations on NSTX from 2004 to 2010. The CHERS diagnostic did not undergo hardware changes (such as number of channels or channel alignment) over this time period that would have altered the interpretation of the measurements used in the database. The database is conditioned to only include times during the I_p flattop, select profiles where the edge T_i and rotation gradients are well resolved, and only consider entries with $Z_{eff} < 3$.

Figure 5(a) summarizes the dependence of the edge $-\nabla T_i$ on the leading order terms of $q_{i,neo}$ as stated in Eq. (5). The Z_{eff}, n_e, and T_i terms are evaluated at the same spatial position as the location of the maximum $-\nabla T_i$ using data from the CHERS and Thomson scattering diagnostics. Z_{eff} is calculated assuming that the deuterium density is $n_D = n_e - 6 n_C$, and the units of n_e, T_i, and I_p are 10^{19} m^{-3}, keV and MA, respectively. The dashed and dashed-dotted curves indicate contours of $-\nabla T_i$ using Eq. (5) and assuming a constant $q_{i,neo}$. The colors in Fig. 5 provide an indication of the most common regimes of operation in NSTX H-modes. The x- and y-axes are divided into 20 increments, and the color contours indicate the number of database entries within each of the 400 cells. The red-orange-yellow region surrounded by the thickest black line (>512 entries) contains 83% of the database and is representative of typical H-mode operation where the maximum edge $-\nabla T_i$ are below 0.15 keV/cm. The blue and red squares correspond to database entries for the discharges shown in Figs. 1–4 where blue is 141125, an ELM-free wide-pedestal H-mode, and red is 141133, an example of EP H-mode. The orange points are from two EP H-mode discharges (134991[13] and 132588[14,15]) with large normalized confinement ($H_{98y2} > 1.6$) that do not apply non-axisymmetric fields.

The database supports that the largest edge $-\nabla T_i$ is realized in regimes that achieve low n_e and Z_{eff}, as shown in Fig. 5(a). The four discharges of interest (square points) illustrate that a small reduction of $n_e^2 Z_{eff}$ can result in a large increase in $-\nabla T_i$ at nearly constant $q_{i,neo}$ in regimes below 0.5 on the x-axis. Conversely, the database indicates that the edge $-\nabla T_i$ scales weakly with $n_e^2 Z_{eff}$ for values greater than 1 along the x-axis.

As shown in Fig. 3, the maximum $-\nabla T_i$ in EP H-mode is nearly aligned with a local minimum in the E_r gradient. It is of interest to investigate if the magnitude of $-\nabla T_i$ is related to the depth of the local E_r well surrounding the local ∇E_r minimum. Figure 5(b) compares the magnitude of $-\nabla T_i$ with the maximum $-\nabla E_r$ realized directly inside (i.e., at smaller ψ_N) of the location of the maximum $-\nabla T_i$ using a database plot similar to Fig. 5(a) where, for each profile, the maximum $-\nabla E_r$ was identified between the location of the top of the carbon toroidal rotation pedestal [Fig. 2(e)] and the location of the maximum $-\nabla T_i$ [Fig. 3(b)]; this region typically spans a few centimeters within the pedestal. The dashed line in Fig. 5(b) is drawn to guide the eye to the approximate linear relationship between the two parameters within the database. The orange datapoints illustrate that the discharges that achieve uniquely large $-\nabla T_i$ also achieve the largest $-\nabla E_r$. The shape of the colored contours in Fig. 5(b) implies that
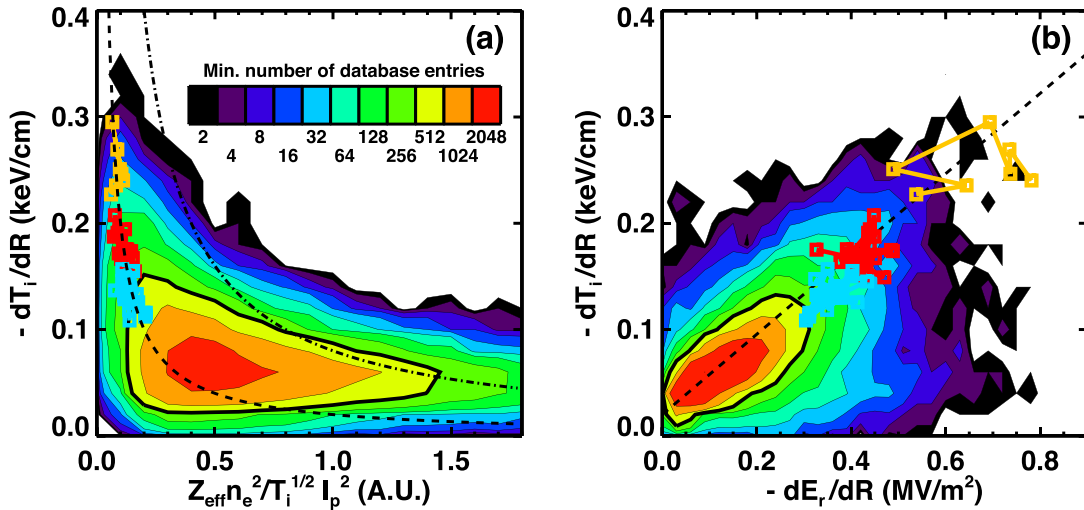

FIG. 4. (a) Leading terms of the neoclassical heat flux in Eq. (4) and (b) the variation in the edge $Z_{eff} n_e^2/T_i^{1/2}$ for the same discharges and time ranges as Figs. 2 and 3.

FIG. 5. Database of maximum edge ion temperature gradient versus (a) leading order terms of neoclassical prediction and (b) maximum E_r gradient inside the location of maximum T_i gradient. Thick black contour encompasses 83% of the database entries. Light blue, red and orange square symbols highlight discharges of interest. The colors of the symbols do not correlate with the contour shading. Dashed and dashed-dotted lines in (a) provide contours of Eq. (5) with constant $q_{i,neo}$. Dashed line in (b) shows approximate linear relationship.

the largest $-\nabla T_i$ will always be accompanied by a large $-\nabla E_r$ inside the location of the maximum $-\nabla T_i$, but the converse relationship is not as likely. This may imply that a large $|\nabla E_r|$ is necessary for producing the peaked density profiles with low edge n_e that facilitate the largest $-\nabla T_i$ by suppressing anomalous particle transport near the top of the pedestal. The impact of $E \times B$ shear on the anomalous transport will be examined in more detail in Sec. V.

The sensitivity of the edge ion temperature gradient to the edge density at low ion collisionality is further demonstrated using a simple 1D-model as shown in Fig. 6. The model solves the time-independent energy transport equations,

$$q_{i,neo} = Q_i - n_D \nu_\varepsilon^{e/i}(T_i - T_e), \qquad (6)$$

$$-n_e \chi_e \nabla T_e = Q_e + n_D \nu_\varepsilon^{e/i}(T_i - T_e), \qquad (7)$$

where Q is the heat flux from all energy sources and sinks excluding ion-electron collisional coupling, which is represented by the right-hand term in both equations ($n_D \nu_\varepsilon^{e/i}(T_i - T_e)$). The model uses a fixed Q for both species assuming a constant net energy density (MW/m^3) from the magnetic axis to R = 1.36 where the magnitude for the ions and electrons is chosen to be consistent with interpretive TRANSP analysis. The magnetic geometry profiles (q, B, κ, etc.) are derived from a magnetic equilibrium from 141133.

The initial n_e and n_C profiles are determined by fitting experimental data [solid black traces in Fig. 6(a)] where the red data points are from EP H-mode phase in discharge 141133 (similar to red data points in Fig. 2). The T_e profile [Fig. 6(b)] is formed assuming a fixed $T_{e,sep}$ and an increase inside the separatrix governed by an inverse scale length (a/L_{Te}) until the top of the pedestal, which is defined as the first point where $T_e/T_i > 0.9$.

The T_i and core T_e profiles are found through an iterative process. On the first iteration, the ion-electron coupling term is set to

zero. In all iterations, T_i at the separatrix is defined to be proportional to $q_{i,neo}$ at the separatrix. The full T_i profile [Fig. 6(c)] inside the separatrix is formed by integrating inward from $T_{i,sep}$ using a simple analytical expression for banana-regime neoclassical $q_{i,neo}$ that is proportional to the large-aspect-ratio approximation given in Ref. 35, similar to Eq. (4). Using the T_i profile, the location of the top of the T_e pedestal is defined and the core T_e profile is computed by integrating inward from this point assuming a constant χ_e. Finally, the ion-electron coupling term is computed using $T_i - T_e$ and the temperature profiles are recomputed with a non-zero coupling term. The iterations continue until the profiles converge to a self-consistent solution.

The simple model has a number of free parameters that can be tuned to get suitable agreement between the modeled temperature profiles (black traces) and the measured profiles (red points). The utility of the model is demonstrating the impact of changing the shape of the density profile using the same assumptions including that the ion energy transport is proportional to the neoclassical thermal transport. A series of calculations were completed for a variety of density profiles where the location and width of the electron density pedestal are changed incrementally [black to red in Fig. 6(a)]. The amplitude of each density profile is adjusted to maintain a constant line-averaged density. Thus, as the density pedestal location shifts outward, the core density is reduced and the density profile becomes broader. The Z_{eff} profile used to compute the black traces is used for all of the other calculations, resulting in similar broadening of the carbon density profiles [Fig. 6(a)]. The iterative process for finding self-consistent temperature profiles is repeated for each choice of the n_e profile.

Peaking the density profiles (red to black) increases the edge $-\nabla T_i$ [Fig. 6(d)] while the core $-\nabla T_i$ is largely unaffected. The model illustrates that the edge $-\nabla T_i$ and core temperatures are increasingly sensitive to small changes in the edge density profile as the edge density decreases. Furthermore, the difference between the T_i and T_e
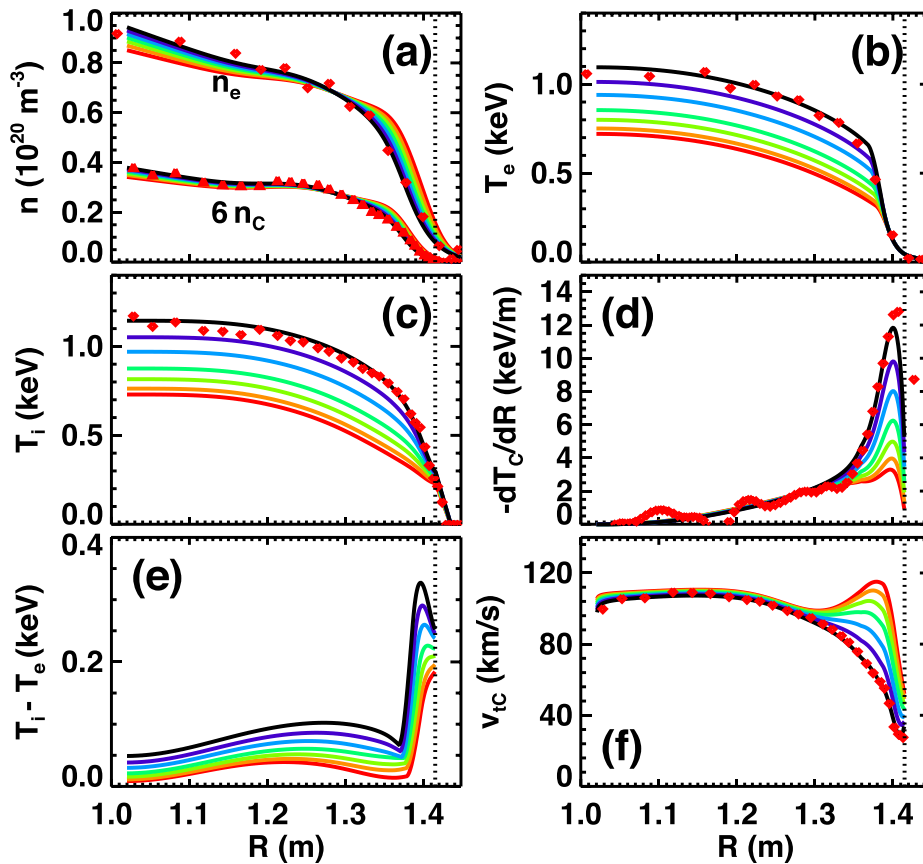
FIG. 6. Results from a 1D transport model compared to EP H-mode datapoints from 141 133 (red points). Each color trace is a single calculation where the (a) electron and ion density profiles are defined and the self-consistent (b) T_e and (c) T_i profiles are computed using assumptions described in the text. The edge (d) ion temperature gradient can increase rapidly for small reduction in the edge density when assuming purely neoclassical ion thermal transport. (e) The difference in the ion and electron temperature profiles increases as the edge density is reduced. (f) Assuming a fixed E_r profile, the carbon toroidal rotation velocity decreases in the edge as the edge density is reduced.

profiles [Fig. 6(e)] becomes larger as the density profile becomes more peaked, consistent with experimental observations [Fig. 2(j)].

Figure 7 reproduces the database plot [Fig. 5(a)] using the profiles from the simple model (solid black) where the dashed and dashed-dotted lines are repeated from Fig. 5(a). The colored vertical dotted lines correspond to the trace colors used in Fig. 6. As the edge density decreases (red to black vertical lines), the $q_{i,neo}$ in the edge region decreases as more of the ion energy is collisionally transferred to the electrons as $T_i - T_e$ increases in the core. Consequently, the results from the simple model qualitatively match the trend of the database results where the maximum of each colored region "falls away" from the dashed-dotted line at smaller values along the x-axis. This qualitative agreement is achieved in the model when including the impact of collisional energy transfer with an increasing $T_i - T_e$ as the edge density is reduced.

Previous publications have noted that the transition between H-mode and EP H-mode is marked by a significant increase in the ion temperature gradient, and a decrease in the edge carbon toroidal rotation.[10,11,15] The profiles shown in Fig. 5 are consistent with this observation, although the difference in the edge rotation between H-mode and EP H-mode is not as large as other examples. The simple model can be used to illustrate that the change in the edge carbon toroidal rotation at the outboard midplane with a larger ion temperature gradient is consistent with a change in the diamagnetic velocity. The black

trace in Fig. 6(f) is chosen to approximately fit the measure carbon toroidal rotation (red points). If the assumption is made that the E_r profile is fixed (purely for illustrative purposes), the carbon toroidal rotation at the outboard midplane varies with the change in the diamagnetic velocity that is driven by the pressure gradient, as shown with the colored traces. As the edge density is reduced (red to black), the magnitude of the toroidal velocity is reduced, qualitatively similar to what has been reported previously. In reality, as shown in Fig. 5, the E_r profile will most likely vary as the edge density and ion temperature profiles change and contribute the observed differences in the edge carbon toroidal rotation.

The $-\nabla T_i$ derived from the 1D model shown in Fig. 6(d) peaks about 2 cm inside the separatrix. The location of the maximum $-\nabla T_i$ relative to the separatrix is most sensitive to the details of the $Z_{eff}n_e^2$ profile [rapidly decreasing toward the separatrix as shown in Fig. 4(b)] and the safety factor (q) profile [rapidly increasing toward the separatrix as shown in Fig. 3(e)] since the form of Eq. (4) has $\nabla T_i \propto Z_{eff}/(q n_e)^2$. The location is also influenced by the decrease in $q_{i,neo}$ as the ions collisionally transfer energy to the colder electrons and the flux-surface volume increases when moving closer to the edge. Discharges that achieve the maximum $-\nabla T_i$ farthest inside the separatrix (for example, see Fig. 5 in Ref. 17) have the smallest edge density gradients, and thus minimize the product of $q n_e$ in a region of smaller q.
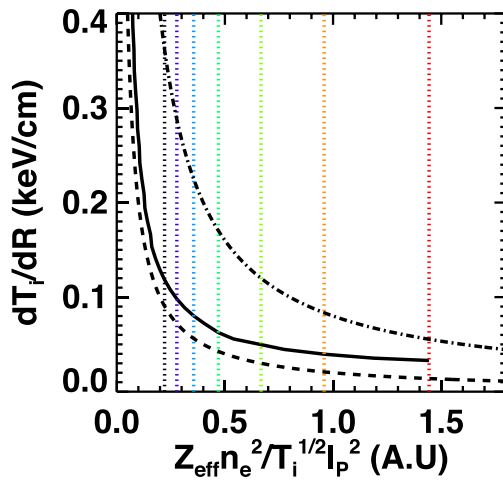
FIG. 7. Reproduction of Fig. 4(a) using the 1-D model results. The vertical dotted lines correspond to the colored traces in Fig. 6. The solid line is the model results and the dash and dashed-dotted lines are reproduced from Fig. 5.

FIG. 8. (a) Divertor D_α emission for EP H-mode (red) and H-mode (blue) discharges. (b) Ratio of maximum neutral density at $T_e = 100$ eV for the two discharges following the second ELM (black) and the ratio of the divertor D_α shown in panel (a) (green dashed). Vertical gray bands highlight two time ranges of interest during the ELM recovery in 141 133.

This section presents evidence that the improved edge ion temperature gradient and energy confinement observed in EP H-mode are a consequence of accessing low edge ion collisionality, particularly by reducing the edge density. Unlike the L–H transition, the improvement in the thermal confinement does not require a change to the nature of the anomalous ion energy transport. However, the next section will demonstrate that the details of the anomalous *particle* transport can play a key role in setting the edge ion collisionality and can lead to a bifurcation in the pedestal solution.

IV. BIFURCATION TO EP H-MODE FOLLOWING AN ELM

EP H-mode was most often observed as an ELM-free period following a large type-I ELM, as shown in Fig. 1. The increase in the global energy confinement evolves over a transport timescale during the ELM recovery to a value that exceeds comparable H-mode conditions. The improvement in the energy confinement is due to the edge density evolving to a new, lower state that drives an improvement in the ion neoclassical confinement. Although EP H-mode was most often observed following a large ELM, examples exist on NSTX of accessing EP H-mode in small ELM or ELM-free periods (see, for example, Fig. 8 of Ref. 17). The discharges that entered EP H-mode in ELM-free regimes typically occur at the largest values of I_p where the lower edge q meant the edge density did not need to be as small to achieve a critically low edge collisionality. Thus, the ELM can help access a state with lower edge collisionality, particularly at lower I_p, but is not a requirement for realizing EP H-mode.

The hypothesis presented in this section is the onset of pressure-driven edge instabilities prior to the full recovery of the neutral density following an ELM can temporarily produce a pedestal solution with lower edge density and larger edge ion temperature gradient. At sufficiently low edge ion collisionality, this temporary solution can produce a bifurcation to a new pedestal state that persists even after the full recovery of the neutral density. Figure 8(a) shows the D_α emission [same traces as Fig. 1(b)] for the EP H-mode discharge (red) and comparable wide-pedestal H-mode (blue). The transient heat flux from
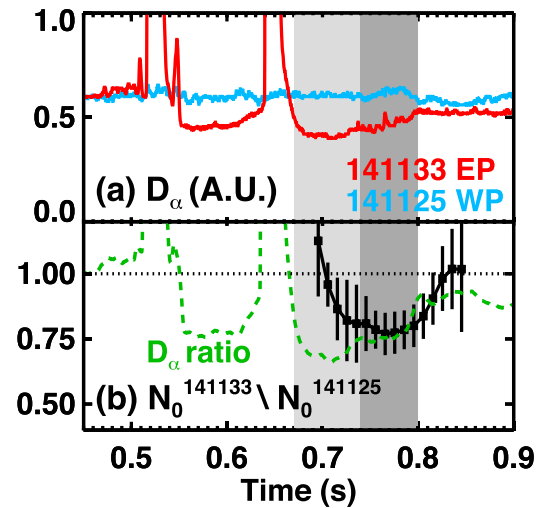
two ELMs in discharge 141133 (red) liberates neutrals from the PFCs, resulting in a spike in the neutral density and D_α emission. Following the large ELMs, the net wall pumping rate increases as the wall deuterium inventory rebuilds resulting in a lower neutral density for about 150 ms after the ELM event as indicated by the dip in the red D_α traces after each ELM.

Recent work has demonstrated that measurements of the passive C^{5+} emission on NSTX can be used to produce an upper bound for the neutral deuterium density (N_0) profile.[36] This upper limit has been shown to be 1.6 ± 0.4 greater than the N_0 derived from D_α signals[37] at $T_e = 100$ eV inside the last-closed-flux-surface. The black points and solid trace in Fig. 8(b) shows the ratio of this upper limit at the location where $T_e = 100$ eV ($\psi_N \sim 0.95$) between the two discharges, while the green dashed line shows the ratio of the divertor D_α signals [red and blue traces in Fig. 8(a)]. The agreement in the timescale of the recovery of both ratios from values near 0.75 to approaching unity provides confidence that the neutral density is temporarily lower for about 200 ms following a large ELM as the wall inventory rebuilds.

The evolution of the local plasma parameters at $\psi_N = 0.9$ ($T_e \sim 140$ eV) for the two discharges shown in Fig. 1 are shown in Fig. 9. The aim of the figure is to identify the timescales for recovery of pedestal parameters from a large ELM in order to provide insight into the pedestal transport and the onset of instabilities. The vertical gray bands in Figs. 8 and 9 highlight two phases of the ELM recovery in the EP H-mode discharge (red traces). During the first phase (light gray), the magnitude of the total pressure gradient [Fig. 9(a)] and ion temperature gradient [Fig. 9(c)] are increasing. The electron temperature gradient [Fig. 9(d)], electron pressure gradient [Fig. 9(b)], and density gradient scale length [Fig. 9(e)] recover quickly after the ELM and are roughly constant during the light gray phase. The evolution of the density gradient scale length prior to this phase is driven primarily by the
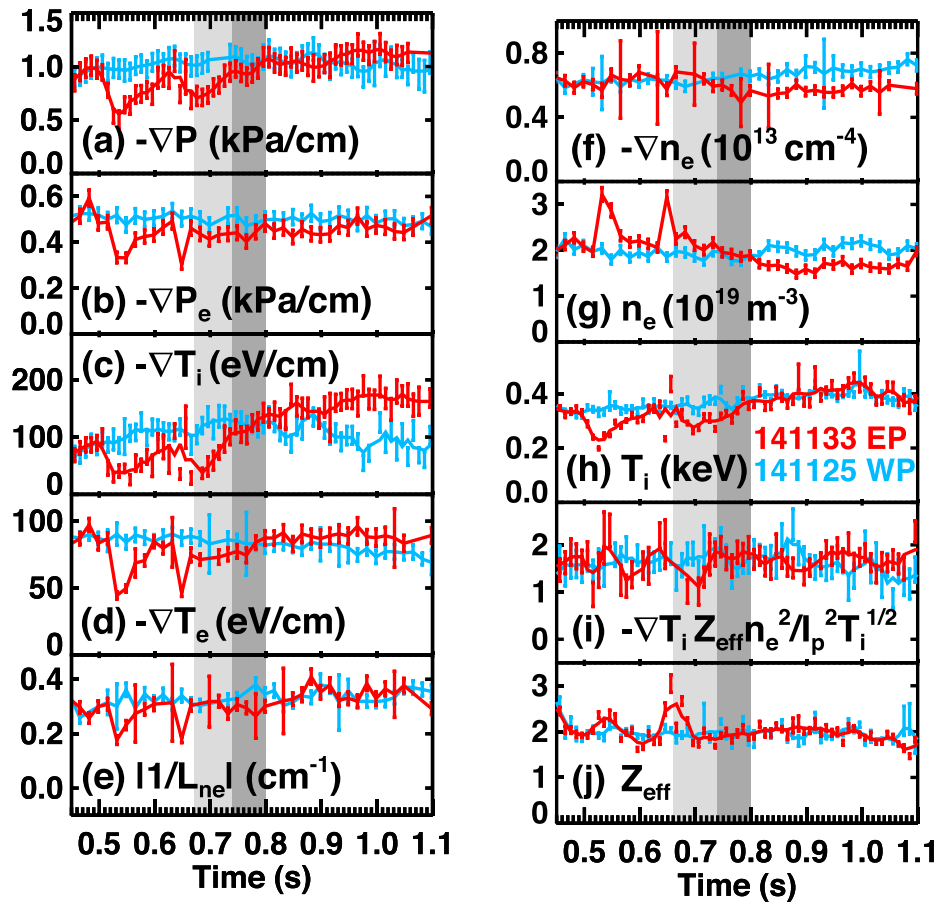
FIG. 9. Evolution of edge parameters at $\psi_N = 0.9$ for EP H-mode (red) and H-mode (blue): (a) negative thermal pressure gradient, (b) negative electron pressure gradient, (c) negative ion temperature gradient, (d) negative electron temperature gradient, (e) absolute value of the inverse electron density scale length, (f) negative electron density gradient, (g) electron density, (h) ion temperature, (i) leading terms of neoclassical heat flux from Eq. (4), and (j) Z_{eff}. Vertical gray bands highlight two time ranges of interest during the ELM recovery shown in Fig. 8.

decreasing density [Fig. 9(g)] since the density gradient [Fig. 9(f)] near the bottom of the pedestal is largely unaffected by the ELM.

Within the second period (dark gray), the local pressure gradient saturates [Fig. 9(a)], indicative of the onset of a pressure driven mode. The density gradient $(-\nabla n_e)$ decreases in this phase to maintain a nearly constant ∇P as the $-\nabla T_i$ [Fig. 9(c)] continues to rise. The EP H-mode phase in 141133 begins at 0.8s (after dark gray phase) when the D_α emission and local T_i [Fig. 9(h)] are fully restored and the edge n_e decreases to a value lower than the H-mode case. In this period, both the local density and the density gradient are reduced to maintain a comparable inverse density scale length to the H-mode discharge [Fig. 9(e)].

Figure 9(i) demonstrates that the leading terms of $q_{i,neo}$ [Eq. (5)] are similar for the two discharges after 0.8 s due to the trade-off in the ion temperature gradient and local density. The local Z_{eff} [Fig. 9(j)] derived from the measurements of n_e and n_C is similar for both discharges. The concurrent increase in the local $-\nabla T_i$ and reduction in the edge density at nearly constant $q_{i,neo}$ is consistent with the analysis presented in Sec. III.

The proposed hypothesis is that the onset of a pressure-driven edge-localized MHD instability before the neutral density has fully recovered leads to a bifurcation in the pedestal transport state (dark gray phase). After the initial saturation of ∇P, the ∇T_i recovery

"overshoots" compared to the pre-ELM and H-mode levels. This overshoot may occur because the temporarily lower neutral density leads to a lower charge exchange loss, and thus a larger ion heat flux that must be transported through the edge. The presumed onset of edge-localized MHD instabilities ensures ∇n_e decreases during the ∇T_i overshoot in order to maintain ∇P consistent with the expectation that the MHD-like modes have an outsized impact on the particle transport compared to the energy transport in the pedestal.[38] This is due to the assumption that neoclassical ion energy transport and anomalous electron energy transport driven by ETG and microtearing modes (MTM) instabilities account for significant energy transport in the pedestal with minimal particle transport while MHD-like instabilities have comparable impact on all channels of transport and most likely account for the bulk of the anomalous particle transport. The lower edge density reinforces the larger $-\nabla T_i$ such that the changes in the temperature and density gradients are "locked in" even after the neutral density recovers ($t > 0.8$ s).

The density profile required to initiate a positive feedback interaction between the neoclassical ion energy transport and an MHD-driven particle transport is illustrated in Fig. 10. The results in Fig. 10 are produced using the simple 1-D transport model described in Sec. III where, for simplicity, the calculations only consider the bottom of the pedestal ($\psi_N > 0.85$) where the T_e is assumed to be
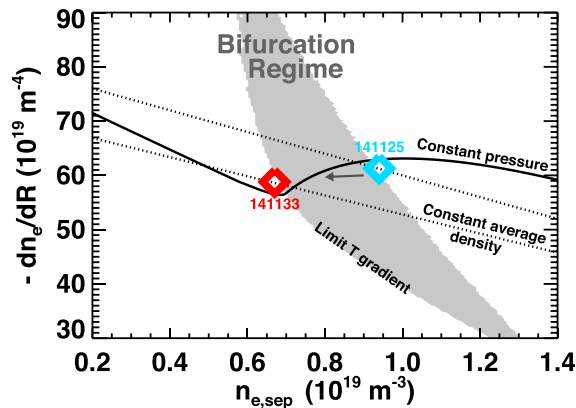
FIG. 10. Bifurcation regime (gray) computed with the simple 1-D model using a range of density profiles defined by the separatrix n_e (x-axis) and n_e gradient (y-axis). Dotted lines are contours of average edge density and solid line is a contour of constant mid-pedestal pressure. Diamonds are representative of wide-pedestal (blue) and EP H-mode (red) discharges.

constant as defined by $T_{e,sep}$ and an inverse scale length a/L_{Te}. Therefore, the model is only solving Eq. (6), where $q_{i,neo}$ is proportional to a simple analytical expression for the neoclassical transport and Q_i is a net energy flux source. For the purpose of the simplified edge calculation, a fixed Q_i (MW/m^2) is assumed at $\psi_N = 0.85$. The calculations consider a range of edge density profiles by defining both $n_{e,sep}$ and ∇n_e and assuming $Z_{eff} = 2$ where fully stripped carbon is the only impurity. For each definition of the n_e profile, the T_i profile for $\psi_N > 0.85$ is computed using the same process described in Sec. III where $T_{i,sep}$ is proportional to $q_{i,sep}$. The converged temperature profiles are used to compute a baseline pressure profile.

Following the baseline calculation, Q_i is increased by 1% and a new T_i profile is computed ($T_{i,over}$) using the same density profiles to simulate a transient increase in the heat flux. Then, using $T_{i,over}$, the density profile is lowered in order to maintain a constant pressure profile ($n_{e,lower}$). Finally, using $n_{e,lower}$ and the original unperturbed Q_i, a third T_i profile is computed ($T_{i,new}$). If $T_{i,new}$ is larger than $T_{i,over}$, then the small temporary increase to Q_i initiates a positive feedback with increasing T_i and decreasing n_e. The important aspect of this interaction is that the density decreases in order to maintain a constant pressure profile at the bottom of the pedestal.

The shaded region in Fig. 10 indicates the density profiles where a small temporary increase in Q_i can initiate a positive feedback. The dotted diagonal lines are contours of constant line-averaged density within $\psi_N > 0.85$ and the solid line is a contour of constant total pressure at $\psi_N = 0.85$. At large $n_{e,sep}$, the pressure contour (solid black) follows the constant line-averaged density contours (dotted) since the temperature profiles do not vary strongly with density in this regime. However, when approaching the right-hand boundary of the bifurcation regime, a constant pressure profile can only be maintained by reducing the average density as the ion temperature gradient becomes sensitive to small changes in the edge density. At sufficiently low $n_{e,sep}$, the right-hand boundary of the bifurcation regime is encountered where a transient increase in Q_i leads to a positive feedback condition.

The left-hand boundary of the bifurcation regime is produced by enforcing a maximum local $-\nabla T_i$; without this arbitrary constraint,

the simple model would not predict a stable pedestal solution after entering the bifurcation regime across the right-hand boundary (in other words, the entire left side of the plot would be shaded). A number of mechanisms, not considered rigorously in this simple model, could damp the positive feedback interaction and produce a stable solution on the left-hand boundary. One mechanism is the growing separation between the core T_i and T_e profiles that leads to larger collisional losses from the ions to the electrons in the core and reduces the edge ion neoclassical heat flux. A second possible mechanism is that the anomalous ion energy flux becomes on the same order as the neoclassical transport and limits the increase in ∇T_i. A third consideration is that the new profiles could lead to an increase in the critical ∇P and/or P_{ped} for the onset of the MHD instabilities responsible for the particle transport allowing stable solutions at higher pedestal pressure. Finally, an increase in the edge Z_{eff} or magnetic geometry changes in the EP H-mode could damp the positive feedback.

The diamond points are representative of the H-mode (blue) and EP H-mode (red) operating points discussed in Fig. 2. The discharges have similar pressure profiles with different trade-offs in the edge temperature and density. The gray arrow indicates the evolution of the discharge along the contour of constant pressure to a new stable state after crossing the right-hand boundary of the bifurcation regime. Repeating the calculations and comparison for locations at smaller ψ_N produces similar agreement with the caveat that some of the assumptions, such as a constant density gradient, are less valid.

To summarize: this section examines the time evolution of pedestal parameters to describe the role a large ELM event can play in triggering a bifurcation of the pedestal to a lower collisionality state. The hypothesis is that the recovery of the pedestal pressure before the recovery of the neutral density can lead to a brief overshoot of $-\nabla T_i$ and a reduction in the edge density due to the onset of MHD-like instabilities. This temporary reduction in the edge density can initiate a bifurcation in the pedestal state where the neoclassical ion transport and anomalous particle transport interact to increase the net particle transport and decrease in the net energy transport. The next section will examine the particle transport mechanisms in the wide-pedestal H-mode that support that MHD-like (KBM and kink-peeling) instabilities are possible mechanisms that can increase the particle transport in the bifurcation process.

V. ANOMALOUS TRANSPORT IN THE WIDE-PEDESTAL AND EP H-MODE

Linear gyrokinetic and resistive MHD calculations demonstrate that the discharges of interest have similar stability properties compared to previous analysis of ELM-free wide-pedestal H-mode on NSTX.[15,17,20] The results are summarized in Fig. 11 where the measurements and calculations are completed for the profiles shown in Fig. 2 (i.e., the saturated EP H-mode phase) and the corresponding time ranges for 141125 (H-mode, blue) and 141133 (EP H-mode, red). Figure 11(a) shows the normalized ion-scale density perturbations ($\delta n/n$) at the outboard midplane peak near the bottom of the pedestal as measured by the Beam Emission Spectroscopy (BES) diagnostic.[39] The BES diagnostic is configured with a single row of eight channels imaging 10 cm above the device midplane and a single column of four channels imaging near $\psi_N \sim 0.85$ between the horizontal row and the device midplane. Each channel has a full-width half-max collection diameter of about 3.75 cm, equating to $\Delta\psi_N \sim \pm 0.1$ in the radial
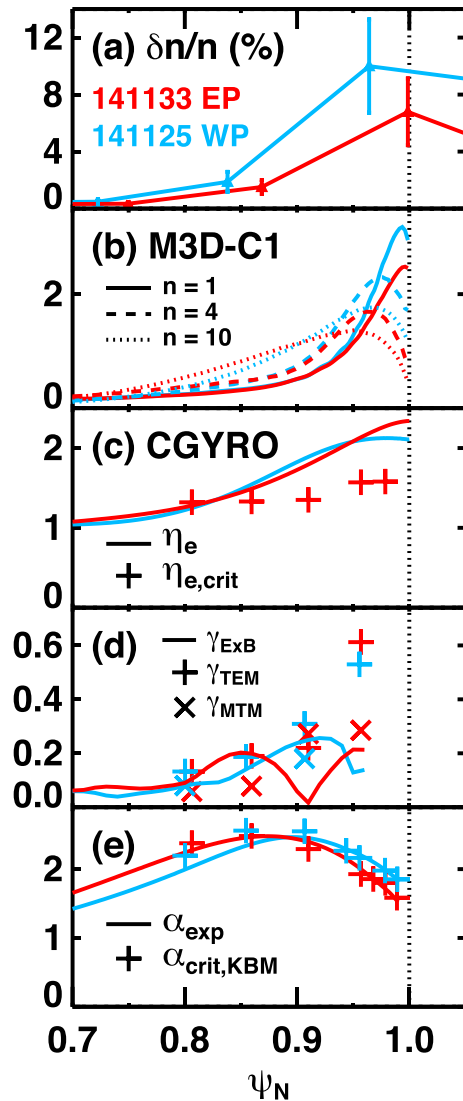
FIG. 11. (a) Average $\delta n/n$ measured by BES corresponding to time range of Fig. 2. Calculations using profiles of Fig. 2: (b) sample of eigenfunctions for unstable modes calculated by single-fluid M3D-C1. CGYRO calculation of (c) experimental η_e (solid) compared to ETG criticality (crosses), (d) linear growth rate of TEM (crosses) and MTM (Xs) compared to E × B shearing rate in normalized units of c_s/a (solid), and (e) experimental α_{MHD} (solid) compared to KBM onset (crosses).

The normalized eigenfunctions for the EP H-mode case (red) are broader than the H-mode case (blue). Initial two-fluid calculations with M3D-C1 indicate that the frequency of the K-P modes is on the order of $n \times 11$ kHz in the lab frame and propagates in the ion diamagnetic drift direction within the lab and plasma frame.

Linear, local gyrokinetic stability calculations using the CGYRO code[41] identify a number of unstable microinstabilities as summarized in Figs. 11(c)–11(e). A spectrum of modes is calculated spanning ion to electron gyroradius scales ($k_\theta\rho_s = 0.05$–100). There is a broad spectrum of unstable electron temperature gradient (ETG) modes at high wavenumbers for $\psi_N > 0.85$. Scans varying the electron temperature gradient are used to calculate a linear threshold ($\eta_{e,crit} \sim 1.3 - 1.5$) that is below the experimental η_e, as shown in Fig. 11(c), and thus predicted to be linearly unstable.

At $k_\theta\rho_s < 0.1$, there are unstable microtearing modes (MTM) or kinetic ballooning modes (KBM), while a broad spectrum of unstable TEM exist up to and beyond $k_\theta\rho_s \sim 1$ across the entire pedestal width. As shown in Fig. 11(d), the growth rates of the TEM are comparable or larger than the MTM growth rates in the edge region. The TEM growth rates are comparable to the local $E \times B$ shearing rates (solid lines) for $\psi_N < 0.85$ and considerably larger near $\psi_N = 0.95$. The inward shift of the E_r well for 141133 (red) compared to 141125 (blue) leads to a wider region where the TEM growth rates exceed the local $E \times B$ shearing rate. Furthermore, the enhanced local shearing rate in 141133 (red) in the region of $0.8 < \psi_N < 0.85$ may lead to the suppression of TEM instabilities that support larger ∇T_e.

Both MTM and ETG instabilities are expected to contribute predominantly to electron thermal transport. Previous nonlinear simulations using GS2[42] in NSTX H-modes[20] illustrate that ETG turbulence can contribute up to a ~1 MW to electron energy transport in similar discharges, suggesting that ETG may play a role in the similarity of the T_e profile outside $\psi_N > 0.85$ in all three discharges [Fig. 2(a)]. In conventional tokamak discharges, nonlinear simulations using GENE indicate that MTM can also contribute electron heat flux levels on the order of the observations[38,43,44] where the nonlinear simulations suggest that MTM is not sensitive to $E \times B$ shear suppression. TEM is expected to contribute to electron thermal transport in addition to particle and ion thermal transport. The ratio of quasi-linear fluxes predicted for TEM ($D/\chi_e = 0.1 - 0.3$, $\chi_i/\chi_e = 1 - 2$) from the CGYRO analysis suggests that TEM could only contribute a fraction of the total electron thermal transport in order to remain consistent with previous interpretative analysis for edge transport in wide-pedestal H-mode using SOLPS where $D/\chi_e < 0.1$.[20]

The entire width of the pedestals in H-mode and EP H-modes is found to be within 10% of the local KBM threshold [Fig. 11(e)]. Transport due to KBM turbulence is expected to produce a stiff pressure gradient through a contribution to all transport channels, where the CGRYO analysis finds that the quasi-linear ratios are similar to the TEM ratios. The KBM threshold shown in Fig. 11(e) is identified by varying electron β in Ampère's equation while keeping the local equilibrium quantities fixed and converting the threshold into the equivalent $\alpha_{MHD} = -2\mu_0 q^2 R\nabla p/B_{unit}^2$. It is noted that if the calculations are repeated with the pressure gradient in the local equilibrium expansion[45] scaled consistently with electron β, the profiles are near second stability where the KBM is completely stabilized, as found in previous analysis in NSTX[20] and other tokamaks.[46,47] Future work is planned

dimension due to the high degree of flux compression at the outboard midplane.

Linear single-fluid resistive MHD calculations with the M3D-C1 code[40] predict a wide range of unstable kink-peeling (K-P) modes up to $n = 20$ for both discharges. The normalized eigenfunctions for a sampling of unstable modes in the single-fluid calculations are presented in Fig. 11(b). The $n = 1$ mode (solid) peaks near the boundary while higher n modes have broader eigenfunctions. The magnitude of the eigenfunctions for the lowest n modes ($n = 1$, solid to $n = 4$, dashed) increases rapidly near the bottom of the pedestal ($\psi_N > 0.9$).

to investigate the self-consistent global KBM stability in the edge of wide-pedestal discharges on NSTX.

The hypothesis presented in Sec. IV is that the particle transport near the bottom of the pedestal ($\psi_N > 0.9$) plays a critical role in establishing and sustaining EP H-mode. The BES diagnostic indicates that the normalized ion-scale density perturbations [Fig. 11(a)] are larger in the edge region compared to the core, consistent with the localization of TEM [Fig. 11(d)] and K-P modes [Fig. 11(b)]. Furthermore, the entire pedestal may operate near a KBM onset threshold [Fig. 11(e)] that limits the local pressure gradient. Energetic particle and MTM instabilities most likely play a role in transport in the core up to the top of the pedestal, while ETG and MTM instabilities are likely responsible for regulating the electron energy transport at the bottom of the pedestal. The linear calculations (Fig. 11) indicate that the stability of the EP H-mode pedestal is similar to wide-pedestal H-mode; thus, the difference in the particle transport is most likely associated with a change in the non-linear interactions rather than a change in the linear mode stability.

Further insight into the nature of the edge instabilities is provided by inspecting the evolution of the density and magnetic fluctuations during the ELM recovery leading to EP H-mode and contrasting these measurements to the wide-pedestal H-mode. Figures 12(a) and 12(c) compare spectrograms of the normalized deuterium density perturbations ($\delta n/n$) measured by a BES diagnostic channel imaging near $\psi_N = 0.85$ for the ELM-free wide-pedestal [Fig. 12(a)] and the EP H-mode discharge [Fig. 12(c)]. Figures 12(b) and 12(d) present a comparison of the toroidal n number of coherent poloidal magnetic field oscillations determined from a toroidal array of magnetic sensors at the outboard midplane. All of the strongest coherent magnetic perturbations propagate co-I_p, which is in the same direction as the measured toroidal flow and in the ion-diamagnetic direction in the laboratory frame. Both discharges have a core tearing mode that begins around 1.1 s with the lowest harmonic near 12 kHz.

The strongest coherent modes in the wide-pedestal H-mode discharge (141125) are below 10 kHz [Fig. 12(a) and 12(b)]. These edge-localized low-n low-frequency modes have been described in previous publications[27,48,49] and are shown to peak in amplitude near the separatrix and induce scrape-off layer (SOL) width broadening in wide-pedestal H-mode. The origin of these modes remains an open question, but they have been shown to correlate with a critical edge rotation (or E_r) gradient[48] in ELM-free discharges. In this example, several $n > 3$ coherent modes are detected, while in other manifestations, a single, strong coherent low-frequency mode is observed.

The light and dark gray shading in Figs. 12(c) and 12(d) highlights the two ELM recovery periods shown in Figs. 8 and 9 for the EP H-mode discharge. Early in the ELM recovery (light gray box), the strongest coherent modes are observed below 20 kHz on both the BES and magnetic diagnostics. The onset of this activity correlates with the saturation of ∇T_e, ∇P_e, and $1/L_{ne}$. Later in the ELM recovery (dark gray time range), the mode amplitudes below 18 kHz abruptly decrease on the BES spectrogram while the mode amplitudes between 18 and 35 kHz increase, which persists into the EP H-mode phase ($t > 0.8$ s). The magnetic analysis identifies diffuse harmonic modes with $n \times 7$ kHz persisting in the EP H-mode phase and the ELM-free H-mode as illustrated by the arrows to the right of Fig. 12(d). This frequency spacing is roughly consistent with the preliminary two-fluid calculations using the M3D-C1 that predicted unstable K-P modes would have a frequency spacing of $n \times 11$ kHz.

The spectrograms of the density and magnetic fluctuations share some common features with ELM-free regimes on conventional-A devices where edge modes provide sufficient particle transport to achieve stationary density profiles with good energy confinement. The detection of a broadband harmonic oscillation (EHO) in the magnetic measurements is similar to the edge-localized modes observed in the wide-pedestal ELM-free QH-mode regime on conventional-A devices;[50] however, no strong signature of these modes is detected on any of the BES channels for the presented discharges, limiting a definitive localization to the edge region. The observation of two frequency bands in the density fluctuations observed in the EP H-mode discharge [Fig. 12(c)] shares some similarities edge-localized modes in the I-mode regime[51] on Alcator C-Mod and ASDEX Upgrade. The broadband density perturbations near 20 kHz in the EP H-mode
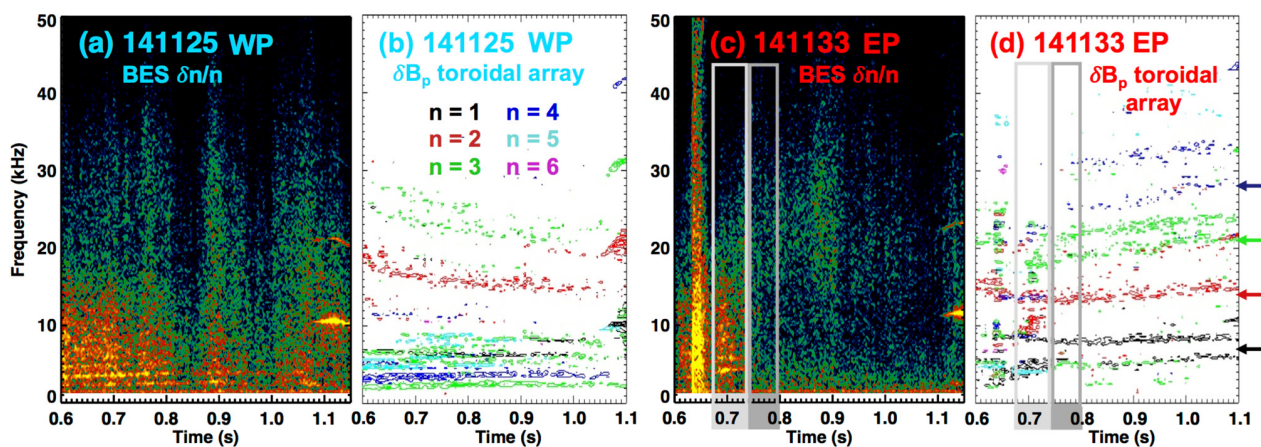

FIG. 12. (a) Spectrogram of BES channel imaging near $\psi_N = 0.88$ and (b) toroidal mode spectrum from a poloidal magnetic field array for wide-pedestal H-mode. Panels (c) and (d) show similar data for EP H-mode where the gray shading indicates two phases of the ELM recovery. The arrows at the right of the image illustrate a 7 kHz spacing of toroidal harmonics.

example may share some connection to the Weakly Coherent Mode (WCM) observed in I-mode that is observed with a low edge density gradient concurrently with large temperature gradients in the pedestal.

The most notable difference between the EP H-mode phase and the ELM-free H-mode discharge is the absence of coherent and broadband low-frequency (<18 kHz) activity. Figure 13 compares the average spectra over specific time ranges in the two discharges for the channel imaging near $\psi_N = 0.85$ (solid lines). The light gray shaded region highlights the significant decrease in the mode amplitudes below 18 kHz in the EP H-mode phase (red) compared to the H-mode example (blue), while the spectra between 18 and 35 kHz is similar (dark gray band). The dashed lines in Fig. 13 show the average spectra for the neighboring BES channel imaging near $\psi_N = 0.75$. The significant reduction of the broadband modes below 80 kHz on this channel localizes these fluctuations to $\psi_N > 0.85$. A small sample of EP H-mode discharges with BES measurements supports that a common feature for these is discharges is the absence of the coherent low-frequency modes and a reduction in the broadband spectrum below 18 kHz relative to the spectrum between 18 and 35 kHz.

Figure 14 presents information derived using the vertical array of four BES channels for the H-mode (blue, left column) and EP H-mode (red, right column) discharges near $\psi_N = 0.85$. The solid lines with diamond points describe the low-frequency density fluctuations between 3 and 18 kHz, while the dashed lines with the square points describe the mid-frequency density fluctuations between 18 and 35 kHz. The vertical gray bands in the panels for discharge 141133 (red) correspond to the ELM recovery phases described with Figs. 8, 9, and 12.

The top panel [Fig. 14(a)] shows the evolution of the normalized magnitude of the deuterium density fluctuations ($\delta n/n$). The low-frequency (solid) perturbations are larger than the mid-frequency perturbations (dashed) in the H-mode discharge (blue) and in the early the ELM recovery of the EP H-mode discharge (red). The $\delta n/n$ for the low-frequency modes drops to the level of the mid-frequency values near the transition to the later ELM-recovery phase and persists into the EP H-mode phase.
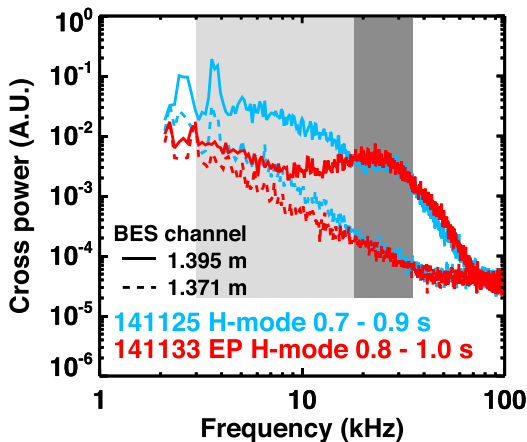

FIG. 14. Characteristics of the density perturbations measured by the vertical array of the BES diagnostic near $\psi_N = 0.87$. Blue and red traces are for the H-mode and EP H-mode discharges, respectively. Solid and dashed lines are for the low- and mid-frequency ranges, respectively. (a) Normalized deuterium density perturbations, (b) poloidal wave number, (c) poloidal correlation length, and (d) group velocity compared to the ExB Doppler velocity (dashed black). Vertical gray bands highlight ELM recovery phases.

The average poloidal wavenumber [k_θ, Fig. 14(b)] for the mid-frequency perturbations is 2–3 times larger than the low-frequency perturbations. The exception is during the ELM recovery where the poloidal wavenumbers are comparable. The poloidal correlation length [L_θ, Fig. 14(c)] of the low-frequency perturbations is greater than the mid-frequency L_θ. The L_θ during the EP H-mode phase is lower than the H-mode discharge for both frequency ranges. This is consistent with previous ELM-free wide-pedestal H-mode database analysis that illustrated that the poloidal correlation length decreases with larger ∇T_i, smaller n_e, and smaller ν_i^* in the steep gradient region.[52]

Figure 14(d) shows the group velocity (v_g) of the density perturbations where positive velocity corresponds to the ion-diamagnetic direction (co-I_p) in the laboratory frame. The vertical black lines in Fig. 12(d) shows the average BES $E \times B$ Doppler shift over the collection region of the BES channel where the height of each line represents the uncertainty. The large flux compression at the outboard midplane increases the sensitivity of the position of the BES sightlines within the

FIG. 13. Average BES cross-power spectra over two separate time ranges for the discharges of interest. Solid lines are for a channel near $\psi_N = 0.87$ while the dashed lines are for a channel near $\psi_N = 0.75$. Gray bands indicate two frequency ranges of interest.
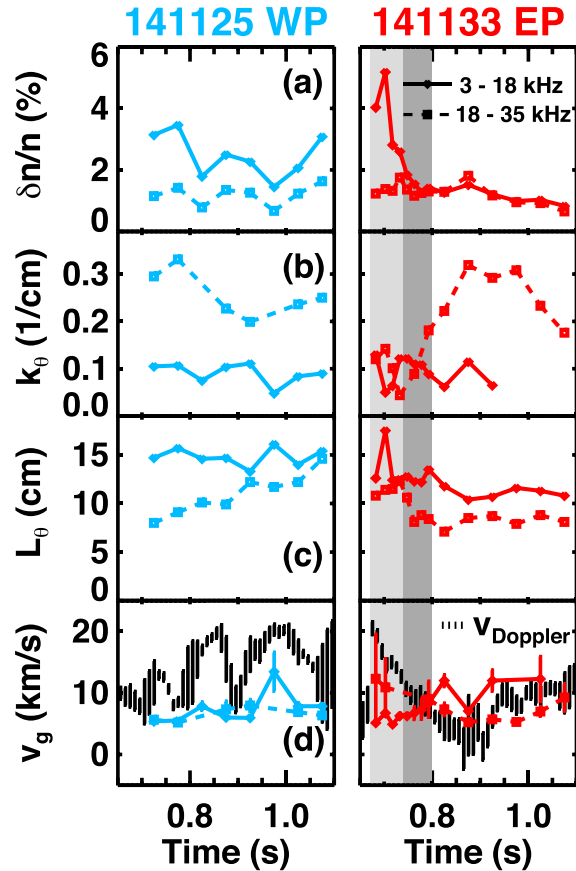
pedestal to small changes to the boundary location. The boundary position for discharge 141133 (red) shifts inward a few millimeters relative to 141125 (blue) during the saturated EP H-mode phase. Therefore, the vertical BES array is centered near $\psi_N = 0.87$ for discharge 141133 while it is further inside ($\psi_N = 0.84$) for discharge 141125 [see data points in Fig. 11(a)]. The vertical array of BES channels is near a region of larger $|\nabla E_r|$; thus, the small shift leads to a difference in the $E \times B$ Doppler velocity.

The group velocity in the H-mode discharge (blue) is similar for both frequency bands and is, on the average, 10 km/s more negative than the Doppler shift velocity, indicating that the density fluctuations propagate in the electron diamagnetic direction within the plasma frame, consistent with TEM and MTM activity. The group velocities during the EP H-mode phase (red traces when t > 0.8 s) have a similar magnitude to the H-mode discharge, but are closer to the Doppler shift velocity, suggesting the fluctuations propagate more toward the ion-diamagnetic direction in the plasma frame, consistent with a greater contribution from MHD-like modes. Furthermore, the low-frequency perturbations (red solid lines) propagate more toward the ion diamagnetic drift direction than the higher frequency perturbations (red dotted lines) in the EP H-mode phase, whereas the propagation direction and velocity are similar for both frequency bands in the wide-pedestal H-mode (blue).

The hypothesis presented in Sec. IV is that an overshoot of $-\nabla T_i$ in the dark gray phase of the recovery leads to an increase in the particle transport necessary to maintain a constant ∇P. The inferred change in the group velocity in the plasma frame by the BES diagnostic is consistent with the onset of TEMs early in the ELM recovery and the onset of an MHD-like instability (KBM and/or kink-peeling) coincident with the saturation of ∇P. However, some of the experimental observations appear, at first glance, to counter the presented hypothesis that the particle transport rate increases in EP H-mode. For example, the density fluctuations below 20 kHz and the poloidal correlation length are reduced coincident with the reduction in the density gradient. Furthermore, no low-frequency coherent modes are detected in the EP H-mode phase in contrast to wide-pedestal H-mode discharges. This may imply that subtle changes in the nature or interaction of the instabilities, such as the cross-phase, are more important in setting the density transport than the mode amplitude. Furthermore, the low-frequency modes have been shown to alter the SOL and the suppression of these modes may lead to a change in the interaction of the SOL and pedestal. Thus, while the presented measurements and calculations indicate that the nature of the pedestal instabilities impacting particle transport do evolve to a new state in EP H-mode, these results do not yet paint a full picture of the role that different transport mechanisms play in the reduction of the edge density.

VI. POTENTIAL FOR EP H-MODE IN NSTX-U

Access to the largest values of normalized confinement in EP H-mode also depends on the plasma stability as the core temperatures increase. For example, the global β_N for the simple model shown in Fig. 6 is approximately five times the central T_i in keV. Therefore, for the black trace in Fig. 6, $T_{i,core} \sim 1.1$ keV and $\beta_N \sim 5.5$. As suggested by the model, a further reduction of the edge density would lead to rapid gains in the core T_i and an increase in the core pressure, increasing the probability of the onset of a global instability if the plasma heating remained constant.

The role of local and global MHD stability in accessing the largest confinement regimes on NSTX is reflected in Fig. 15. The data points are reproduced from Fig. 10(a) in Ref. 17 where the normalized global confinement ($H_{98y,2}$) is plotted vs the q_{95} for a database of discharges. The database includes two entries for every discharge: one time point in the presumed EP H-mode phase following an ELM recovery (red and orange points) and one time point from the H-mode phase preceding the ELM (blue points). The previous analysis identified EP H-mode phases using a critical threshold in the maximum edge ion temperature gradient: $-\nabla T_i > 0.09$ keV/m. However, a threshold that reflects the expecting scaling of the gradients with I_p^2 [consistent with Eq. (5)] is found to better identify the highest confinement discharges,

$$-\Delta T_i(\text{keV/cm}) > 0.145 \left[I_p(\text{MA}) \right]^2. \quad (8)$$

The red points in Fig. 15 exceed this more restrictive threshold, while the orange points were considered EP H-mode discharges in Ref. 17, but do not satisfy this new criterion and are considered H-mode discharges using the threshold in Eq. (8). The red dotted line in Fig. 15 is provided to guide the eye as an approximate minimum for the red points for $q_{95} < 10$. The maximum normalized confinement of the H-mode discharges increases with q_{95}, indicative of the weaker scaling of the energy confinement with I_p compared to the $H_{98y,2}$ confinement scaling that was observed on NSTX.[9,53]

The cloud of blue and orange entries with $q_{95} \sim 6.5$ illustrates that operating at large I_p provided consistent access to large ion temperature gradients in H-mode, consistent with the neoclassical scaling in Eq. (5). These discharges are realized at $I_p > 1$ MA with the appearance of the large $-\nabla T_i$ early in the discharge before the q-profile has relaxed. The maximum energy confinement in EP H-mode discharges (red points) with $q_{95} < 8$ tends to be limited by tearing-mode MHD that appears with the entry of low-order rational surfaces ($q = 3/2$ or 1). Figure 2 of Ref. 17 presents examples of these early, short-lived EP H-modes that terminate after the appearance of MHD activity.

Conversely, operating at $q_{95} > 10$ with $I_p < 0.85$ MA showed little difference in the maximum confinement compared to H-mode. These EP H-mode scenarios were less reproducible since they required uniquely lower edge density in order to achieve the significant increase in the ion temperature gradients at lower I_p. These EP H-mode phases were more likely to end with the appearance of an ELM or a global instability as the central pressure and β_N increased, leading to a return to H-mode edge gradients. For these reasons, the highest normalized
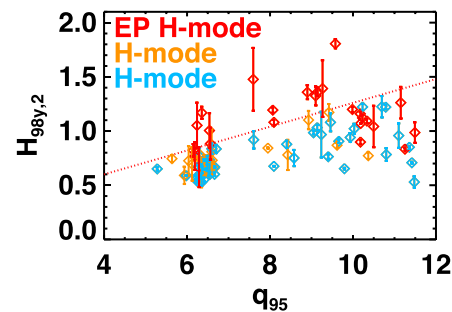

FIG. 15. Database of normalized confinement plotted against q_{95}, adapted from Ref. 15.

confinement in EP H-mode discharges occurs with $q_{95} \sim 9$ where I_p is large enough that the discharges remain below pedestal and global stability limits at elevated confinement and small enough to delay the entry of the $q_0 = 1$ surface until near the end of the discharge. Discharge 141133 (red traces, Fig. 1) is an example of an EP H-mode discharge with $I_p[MA]/B_T[T] = 2$, $q_{95} = 9$ and $H_{98y,2} \sim 1.35$ that operates in this range.

A number of enhancements to NSTX-U compared to NSTX are projected to increase the flexibility for accessing and sustaining EP H-mode. NSTX-U will improve the coverage of evaporative lithium via the addition of an upward-facing evaporator for the upper divertor that has the potential to improve the control of the edge neutral density, particularly in double-null shapes, and will also add a real-time lithium powder injection system. Furthermore, an improved PFC baking system and installation of fish-scaled divertor tiles may reduce the impurity influx. In addition, an expansion of the 3D field coil power supplies will increase the flexibility in tailoring the field spectrum as an actuator for edge transport and stability control.

NSTX-U will approximately double the toroidal field strength (1 T) and I_p (2 MA) compared to the EP H-mode discharges with the largest normalized confinement on NSTX (0.45 T, 0.9 MA). Consequently, the target q-profiles for high-performance discharges on NSTX-U with $I_p/B_T = 2$ MA/T are consistent with the best EP H-mode discharges on NSTX. However, NSTX-U will be better equipped to achieve the high confinement state concurrently with a relaxed q-profile that is stable to global MHD due to the addition of a second, more tangential neutral beam injection (NBI) system on NSTX-U that will broaden the beam-driven current profile and assist in maintaining $q_0 > 3/2$. Additionally, improved alignment and rigidity of the central column on NSTX-U will reduce the magnitude of error fields that were conducive to seeding low-order MHD as $q_{min} \rightarrow 1$.

The doubling of the plasma current requires roughly doubling the core temperature and operating with a similar Greenwald density fraction in order to achieve a similar β_N to NSTX. Using the simple 1-D model with twice the magnetic field, heating and density suggests that the EP H-mode bifurcation could be accessed at larger values of edge Greenwald fraction (i.e., less peaked density profiles) due to the decreasing collisionality with larger edge T_i ($v_i^* \sim T_i^{-1/2}$). Furthermore, the model suggests that there is increased potential for exceeding the normalized confinement of EP H-mode on NSTX through additional peaking of the density (for example, maintaining a similar edge density, but doubling the core density).

Although the potential for achieving EP H-mode on NSTX-U appears promising, there remain a number of open questions in the projections. One question is whether the maximum edge $-\nabla T_i$ will be limited by anomalous transport as the neoclassical thermal diffusivity continues to decrease at lower collisionality. Another question is how the anomalous electron thermal transport will scale as the field strength increases and the electron collisionality decreases. Within the simple model, the eventual maximum normalized confinement is dictated by the choices in the electron thermal transport since the core T_i and T_e are tightly coupled at large f_{GW}. Finally, the variation of the structure of the E_r profile with changes to the field strength, aspect ratio and mix of neutral beam injection, and the role of $E_r \times B$ on the energy and density transport is an important unknown aspect of the projections for NSTX-U.

A significant challenge for future compact tokamak reactor designs is dealing with the large heat flux delivered to the PFCs. The leading technical solution is to operate at sufficient divertor neutral pressure to achieve a detached divertor leg. This requirement may be at odds with the EP H-mode requirement that aims to minimize the edge density relative to the core. The next generation of MA-class ST experiments are pursuing technical solutions that may accommodate the competing requirements for managing divertor heat flux and maintaining a peaked density profile. NSTX-U aims to transition the device within the decade to test an open divertor with liquid lithium PFCs that offer combined resilience to steady-state and transient heat flux while pumping hydrogenic species and limiting the sputtering of high-Z surfaces. MAST-U will operate with highly baffled divertors, permitting the decoupling of the large divertor neutral pressure needed for detachment from the main chamber neutral pressure.[54]

VII. SUMMARY AND FUTURE RESEARCH

EP H-mode is a promising regime for compact tokamak concepts since it achieves enhanced thermal confinement in an ELM-free regime with increased edge particle transport. One unresolved challenge is demonstrating EP H-mode with stationary density and current profiles. The new capabilities on NSTX-U, such as a more tangential NBI, higher field, improved evaporative lithium coverage, and longer inductive pulses will provide new opportunities to resolve this challenge and further evaluate if EP H-mode is an attractive regime for a compact fusion reactor. A second challenge is gaining sufficient understanding of EP H-mode to confidently design and operate future devices that optimize access and sustainment.

This paper presents evidence that the improvement in the thermal confinement in EP H-mode is driven by the reduction in the ion neoclassical thermal transport at sufficiently small edge density. EP H-mode was most often observed on NSTX following a large ELM where the pedestal recovers to a larger value compared to a matched ELM-free discharge. The transition to a new transport solution is attributed to a positive feedback interaction between a reduction in the neoclassical ion thermal transport and an increase in MHD-driven particle transport. This bifurcation process is in contrast to the L-H transition where the suppression of anomalous transport concurrently improves particle and energy transport. It is hypothesized that the important feature in the ELM recovery is the onset of the MHD-like instability prior to the full recovery of the neutral density after the ELM.

Section V describes the anomalous processes that can play a role in the particle transport, including MHD-like instabilities such as KBM and kink-peeling (K-P) instabilities. The linear calculations and ion-scale turbulence measurements by the BES system support that the dominant ion-scale instabilities in the edge transition from being TEM-like to MHD-like in the EP H-mode phase. This is consistent with the "transport fingerprints"[38] where MHD-like instabilities have a larger impact on the electron and deuterium diffusivity compared to TEM. Future work will leverage non-linear gyrokinetic calculations and non-linear, two-fluid MHD calculations to further clarify this hypothesis. In addition, improved resolution and coverage of fluctuation diagnostics, such as BES, on NSTX-U will provide critical measurements for validating the calculations.

Some parallels between the wide-pedestal and EP H-mode on NSTX can be drawn to enhanced confinement regimes on

conventional-A devices. The enhanced ion thermal confinement is similar to high-β_p regimes on conventional-A tokamaks. In both cases, ITG modes are stabilized by flux compression from large magnetic shear resulting in large-radius ITBs that are independent of $E \times B$ shear leading to ion thermal transport being reduced to the neoclassical level. These high-β_p regimes exhibit enhanced thermal confinement concurrently with density near the Greenwald density limit and broad pressure profiles that support high edge bootstrap current fraction.

The ELM-free H-mode and EP H-mode states also share some similarities with stationary ELM-free regimes, such as QH-mode. QH-mode achieves a stationary ELM-free state via particle transport from either a coherent EHO or broadband turbulence where, at low edge collisionality, a saturated kink-peeling instability is predicted to contribute to the transport.[50] The discharges presented in this paper hint at a saturated EHO-like instability in the magnetic measurements (Fig. 12) with about 10 kHz frequency separation between the harmonics. The existence of saturated K-P modes in the ELM-free wide-pedestal and ELM-free regimes is consistent with the linear resistive MHD calculations using M3D-C1 shown in Fig. 11(b). These modes may be responsible for the enhanced edge particle transport predicted to play a role in sustaining EP H-mode. The nature of the EHO on conventional-A devices is sensitive to the $E \times B$ shear; therefore, the improved control over the edge rotation shear on NSTX-U using the new, more tangential neutral beams and improved 3D field coils will facilitate the optimization of ELM-free regimes on NSTX-U.

Operation at a low aspect ratio provides a route to a compact fusion reactor system by simultaneously achieving the high-confinement and bootstrap properties of high-β_p operation with operation at large-β_T. EP H-mode is the realization of enhance ion thermal confinement with a rapid reduction of neoclassical diffusion with ν_i^* in a regime with suppressed ITG instabilities. The resulting increase in the edge ion temperature gradient can lead to a positive feedback interaction with a pressure-driven edge instability that lowers the edge density and further reduces ν_i^*. The next generation of ST devices, including NSTX-U, will access a wider range of operational conditions to produce regimes with low edge ion collisionality and investigate if EP H-mode can be accessed and sustained in stationary scenarios without large ELMs.

ACKNOWLEDGMENTS

DATA AVAILABILITY

The digital data for this paper can be found in: http://arks.princeton.edu/ark:88435/dsp016h440w39j.

REFERENCES

[1]J. E. Menard, T. Brown, L. El-Guebaly, M. Boyer, J. Canik, B. Colling, R. Raman, Z. Wang, Y. Zhai, P. Buxton *et al.*, Nucl. Fusion **56**, 106023 (2016).

[2]B. N. Sorbom, J. Ball, T. R. Palmer, F. J. Mangiarotti, J. M. Sierchio, P. Bonoli, C. Kasten, D. A. Sutherland, H. S. Barnard, C. B. Haakonsen *et al.*, Fusion Eng. Des. **100**, 378 (2015).

[3]J. E. Menard, S. Gerhardt, M. G. Bell, J. Bialek, A. Brooks, J. M. Canik, J. Chrzanowski, M. Denault, L. Dudek, D. A. Gates *et al.*, Nucl. Fusion **52**(39), 083015 (2012).

[4]A. M. Garofalo, X. Z. Gong, S. Y. Ding, J. Huang, J. McClenaghan, C. K. Pan, J. Qian, Q. L. Ren, G. M. Staebler, J. Chen *et al.*, Plasma Phys. Controlled Fusion **60**, 014043 (2018).

[5]Y. Kamada, Nucl. Fusion **41**, 1311 (2001).

[6]J. Connor, T. Fukuda, X. Garbet, C. Gormezano, V. Mukhovatov, and M. Wakatani, the I. D. Group, the I. T. G. on Transport, and I. B. Physics. Nucl. Fusion **44**, R1 (2004).

[7]J. McClenaghan, A. M. Garofalo, L. L. Lao, D. B. Weisberg, O. Meneghini, S. P. Smith, B. C. Lyons, G. M. Staebler, S. Y. Ding, J. Huang *et al.*, Nucl. Fusion **60**, 046025 (2020).

[8]A. M. Garofalo, X. Gong, B. A. Grierson, Q. Ren, W. M. Solomon, E. J. Strait, M. A. Van Zeeland, C. T. Holcomb, O. Meneghini, S. P. Smith *et al.*, Nucl. Fusion **55**, 123025 (2015).

[9]S. M. Kaye, R. E. Bell, D. Gates, B. P. Leblanc, F. M. Levinton, J. E. Menard, D. Mueller, G. Rewoldt, S. A. Sabbagh, W. Wang *et al.*, Phys. Rev. Lett. **98**, 175002 (2007).

[10]M. Valovič, R. Akers, M. De Bock, J. McCone, L. Garzotti, C. Michael, G. Naylor, A. Patel, C. M. Roach, R. Scannell *et al.*, Nucl. Fusion **51**, 073045 (2011).

[11]Y. Ren, W. X. Wang, W. Guttenfelder, S. M. Kaye, J. Ruiz-Ruiz, S. Ethier, R. Bell, B. P. LeBlanc, E. Mazzucato, D. R. Smith *et al.*, Nucl. Fusion **60**, 026005 (2020).

[12]R. Maingi, R. E. Bell, B. P. LeBlanc, D. A. Gates, S. M. Kaye, J. E. Menard, S. A. Sabbagh, and H. Yuh, J. Nucl. Mater. **390–391**, 440 (2009).

[13]R. Maingi, R. Bell, J. Canik, S. Gerhardt, S. Kaye, B. LeBlanc, T. Osborne, M. Bell, E. Fredrickson, K. Lee *et al.*, Phys. Rev. Lett. **105**, 135004 (2010).

[14]R. Maingi, T. H. Osborne, M. G. Bell, R. E. Bell, D. P. Boyle, J. M. Canik, A. Diallo, R. Kaita, S. M. Kaye, H. W. Kugel *et al.*, J. Nucl. Mater. **463**, 1134 (2015).

[15]M. Coury, W. Guttenfelder, D. R. Mikkelsen, J. M. Canik, G. P. Canal, A. Diallo, S. Kaye, G. J. Kramer, and R. Maingi, Phys. Plasmas **23**, 062520 (2016).

[16]V. A. Soukhanovskii, W. R. Blanchard, J. K. Dong, R. Kaita, H. W. Kugel, J. E. Menard, T. J. Provost, R. Raman, A. L. Roquemore, and P. Sichta, Fusion Sci. Technol. **75**, 1 (2019).

[17]S. P. Gerhardt, J. M. Canik, R. Maingi, D. Battaglia, R. E. Bell, W. Guttenfelder, B. P. LeBlanc, D. R. Smith, H. Yuh, and S. Sabbagh, Nucl. Fusion **54**, 083021 (2014).

[18]J. M. Canik, R. Maingi, S. Kubota, Y. Ren, R. E. Bell, J. D. Callen, W. Guttenfelder, H. W. Kugel, B. P. Leblanc, T. H. Osborne *et al.*, Phys. Plasmas **18**, 056118 (2011).

[19]R. Maingi, T. Osborne, B. LeBlanc, R. Bell, J. Manickam, P. Snyder, J. Menard, D. Mansfield, H. Kugel, R. Kaita *et al.*, Phys. Rev. Lett. **103**, 075001 (2009).

[20]J. M. Canik, W. Guttenfelder, R. Maingi, T. H. Osborne, S. Kubota, Y. Ren, R. E. Bell, H. W. Kugel, B. P. LeBlanc, and V. A. Souhkanovskii, Nucl. Fusion **53**, 113016 (2013).

[21]J. M. Canik, R. Maingi, V. A. Soukhanovskii, R. E. Bell, H. W. Kugel, B. P. Leblanc, and T. H. Osborne, J. Nucl. Mater. **415**, S409 (2011).

[22]L. Frassinetti, M. G. Dunne, U. Sheikh, S. Saarelma, C. M. Roach, E. Stefanikova, C. Maggi, L. Horvath, S. Pamela, E. De La Luna *et al.*, Nucl. Fusion **59**, 076038 (2019).

[23]V. A. Soukhanovskii, R. E. Bell, C. Bush, R. Kaita, H. W. Kugel, B. P. LeBlanc, R. Maingi, R. Raman, and A. L. Roquemore, J. Nucl. Mater. **390–391**, 516 (2009).

[24]J. M. Canik, R. Maingi, T. E. Evans, R. E. Bell, S. P. Gerhardt, H. W. Kugel, B. P. LeBlanc, J. Manickam, J. E. Menard, T. H. Osborne *et al.*, Nucl. Fusion **50**, 034012 (2010).

[25]S. P. Gerhardt, D. Gates, S. M. Kaye, R. Maingi, J. E. Menard, S. a Sabbagh, V. Soukhanovskii, M. G. Bell, R. E. Bell, J. M. Canik *et al.*, Nucl. Fusion **51**, 073031 (2011).

[26]J. E. Menard, R. E. Bell, D. a Gates, S. P. Gerhardt, J.-K. Park, S. a Sabbagh, J. W. Berkery, A. Egan, J. Kallman, S. M. Kaye *et al.*, Nucl. Fusion **50**, 045008 (2010).

[27]A. C. Sontag, J. M. Canik, R. Maingi, J. Manickam, P. B. Snyder, R. E. Bell, S. P. Gerhardt, S. Kubota, B. P. LeBlanc, D. Mueller *et al.*, Nucl. Fusion **51**, 103022 (2011).

[28]B. P. LeBlanc, R. E. Bell, D. W. Johnson, D. E. Hoffman, D. C. Long, and R. W. Palladino, Rev. Sci. Instrum. **74**, 1659 (2003).

[29]R. E. Bell and R. Feder, Rev. Sci. Instrum. **81**, 10D724 (2010).

[30]F. Scotti, V. A. Soukhanovskii, R. E. Bell, S. Gerhardt, W. Guttenfelder, S. Kaye, R. Andre, A. Diallo, R. Kaita, B. P. Leblanc *et al.*, Nucl. Fusion **53**, 083001 (2013).

[31]M. Podestà, R. E. Bell, A. Diallo, B. P. Leblanc, and F. Scotti, Nucl. Fusion **52**, 033008 (2012).

[32]F. M. Levinton and H. Yuh, Rev. Sci. Instrum. **79**, 10F522 (2008).

[33]S. R. R. Haskey, B. A. A. Grierson, C. Chrystal, A. Ashourvan, K. H. H. Burrell, R. J. J. Groebner, E. A. A. Belli, L. Stagner, D. J. J. Battaglia, T. Stoltzfus-Dueck *et al.*, Plasma Phys. Controlled Fusion **60**, 105001 (2018).

[34]J. D. Callen, *Fundamental Processes in Plasmas* (University of Wisconsin, 2006), Chap. 2.

[35]J. Wesson, *Tokamaks*, 3rd ed. (Oxford Science Publications, 2004).

[36]R. E. Bell, F. Scotti, A. Diallo, B. P. Leblanc, M. Podesta, and S. A. Sabbagh, in *APS Div. Plasma Phys. Meet. Abstr.* (2017), p. PP11.062.

[37]D. P. Stotler, F. Scotti, R. E. Bell, A. Diallo, B. P. LeBlanc, M. Podestà, A. L. Roquemore, and P. W. Ross, Phys. Plasmas **22**, 082506 (2015).

[38]M. Kotschenreuther, X. Liu, D. R. Hatch, S. Mahajan, L. Zheng, A. Diallo, R. Groebner, J. C. Hillesheim, C. F. Maggi, C. Giroud *et al.*, Nucl. Fusion **59**, 096001 (2019).

[39]D. R. Smith, R. J. Fonck, G. R. McKee, and D. S. Thompson, Rev. Sci. Instrum. **83**, 10D502 (2012).

[40]N. M. Ferraro, S. C. Jardin, L. L. Lao, M. S. Shephard, and F. Zhang, Phys. Plasmas **23**, 056114 (2016).

[41]J. Candy, E. A. Belli, and R. V. Bravenec, J. Comput. Phys. **324**, 73 (2016).

[42]M. Kotschenreuther, G. Rewoldt, and W. M. Tang, Comput. Phys. Commun. **88**, 128 (1995).

[43]D. R. Hatch, M. Kotschenreuther, S. Mahajan, P. Valanju, F. Jenko, D. Told, T. Görler, and S. Saarelma, Nucl. Fusion **56**, 104003 (2016).

[44]D. R. Hatch, M. Kotschenreuther, S. Mahajan, P. Valanju, and X. Liu, Nucl. Fusion **57**, 064001 (2017).

[45]J. Candy, Plasma Phys. Controlled Fusion **51**, 105009 (2009).

[46]S. Saarelma, M. N. A. Beurskens, D. Dickinson, L. Frassinetti, M. J. Leyland, and C. M. Roach, Nucl. Fusion **53**, 123012 (2013).

[47]S. Saarelma, J. Martin-Collar, D. Dickinson, B. F. McMillan, and C. M. Roach, Plasma Phys. Controlled Fusion **59**, 064001 (2017).

[48]J. K. Park, R. J. Goldston, N. A. Crocker, E. D. Fredrickson, M. G. Bell, R. Maingi, K. Tritz, M. A. Jaworski, S. Kubota, F. Kelly *et al.*, Nucl. Fusion **54**, 043013 (2014).

[49]K. F. Gan, J. W. Ahn, T. K. Gray, S. J. Zweben, E. D. Fredrickson, F. Scotti, R. Maingi, J. K. Park, G. P. Canal, V. A. Soukhanovskii *et al.*, Nucl. Fusion **57**, 126053 (2017).

[50]X. Chen, K. H. Burrell, T. H. Osborne, K. Barada, N. M. Ferraro, A. M. Garofalo, R. J. Groebner, G. R. McKee, C. C. Petty, M. Porkolab *et al.*, Nucl. Fusion **57**, 086008 (2017).

[51]A. E. Hubbard, T. Osborne, F. Ryter, M. Austin, L. Barrera Orte, R. M. Churchill, I. Cziegler, M. Fenstermacher, R. Fischer, S. Gerhardt *et al.*, Nucl. Fusion **56**, 086003 (2016).

[52]D. R. Smith, R. J. Fonck, G. R. McKee, D. S. Thompson, R. E. Bell, A. Diallo, W. Guttenfelder, S. M. Kaye, B. P. Leblanc, and M. Podesta, Phys. Plasmas **20**, 055903 (2013).

[53]S. M. M. Kaye, S. Gerhardt, W. Guttenfelder, R. Maingi, R. E. E. Bell, A. Diallo, B. P. P. LeBlanc, M. Podesta, H. Search, C. Journals *et al.*, Nucl. Fusion **53**, 063005 (2013).

[54]W. Morris, J. R. Harrison, A. Kirk, B. Lipschultz, F. Militello, D. Moulton, and N. R. Walkden, IEEE Trans. Plasma Sci. **46**, 1217 (2018).